Geophysical Prospecting

"Rock-physics - From microstructure to seismic signatures"

Integrating facies-based Bayesian inversion and supervised machine learning for petrofacies characterisation in the Snadd Formation of the Goliat Field, SW Barents Sea.

Journal:	*Geophysical Prospecting*
Manuscript ID	GP-2017-0155.R2
Manuscript Type:	Special Issue
Date Submitted by the Author:	19-Apr-2018
Complete List of Authors:	Dzekamelive Yenwongfai, Honore; Universitetet i Oslo Det Matematisk-naturvitenskapelige Fakultet, Geoscience; Mondol, Nazmul; University of Oslo, Department of Geosciences Lecomte, Isabelle; Universitetet i Bergen Det Matematisk-naturvitenskapelige Fakultet, Earth Science; Faleide, Jan Inge; University of Oslo, Department of Geosciences Leutscher, Johan; EniNorge,
Keyword:	Reservoir characterization, Rock physics, Inversion

EAGE Publications B.V., PO Box 59, 3990 DB, Houten, The Netherlands

Integrating facies-based Bayesian inversion and supervised machine learning for petrofacies characterisation in the Snadd Formation of the Goliat Field, SW Barents Sea.

Honoré Yenwongfai [2,1], Nazmul Haque Mondol [1,3], Isabelle Lecomte [4], Jan Inge Faleide [1], Johan Leutscher [5]

[1] *University of Oslo,* [2] Statoil ASA, [3] Norwegian Geotechnical Institute, [4] University of Bergen, [5]Eni Norge.
Contact email: hyen@statoil.com

ABSTRACT

Seismic petrofacies characterisation in low net-to-gross reservoirs with poor reservoir properties such as the Snadd Formation in the Goliat field, requires a multidisciplinary approach. This is especially important when the elastic properties of the desired petrofacies significantly overlap. Pore fluid corrected end-member sand and shale depth trends have been used to generate stochastic forward models for different lithology and fluid combinations in order to assess the degree of separation of different petrofacies. Subsequently, a spectral decomposition and blending of selected frequency volumes reveal some seismic fluvial geomorphological features. We then jointly inverted for impedance and facies within a Bayesian framework using facies-dependent rock physics depth trends as input. The results from the inversion are then integrated into a supervised machine learning neural network for effective porosity discrimination. Probability density functions derived from stochastic forward modelling of end-member depth trends show a decreasing seismic fluid discrimination with depth. Spectral decomposition and blending of selected frequencies reveal a dominant NNE trend compared to the regional SE – NW progradational trend, and a local E-W trend potentially related to fault activity at branches of the Troms-Finnmark Fault Complex. The facies-based inversion captures the main reservoir facies within the limits of the seismic bandwidth. Meanwhile the effective porosity predictions from the multilayer feedforward neural network are consistent with the inverted facies model, and can be used to qualitatively highlight the cleanest regions within the inverted facies model. A combination of facies-based inversion and neural network improves the seismic reservoir delineation of the Snadd Formation in the Goliat Field.

Keywords: Inversion, rock physics, facies, reservoir characterisation, neural network

INTRODUCTION

The Norwegian Barents Shelf (NBS) is a frontier hydrocarbon exploration province when compared to the other parts of the Norwegian Continental Shelf (NCS) such as North Sea and Norwegian Sea. The NBS has a far more complex burial history, with differential amounts of uplift and erosion within the different basins, platform areas and local highs. Uplift and erosion introduce additional challenges and uncertainties when evaluating the petroleum system with respect to cap rock integrity, source rock maturation, and overconsolidation of the target reservoirs with respect to the present day depths. Understanding and constraining rock physics depth trends is crucial in areas with such a complex burial history.

The Goliat Field is located about 85 km southeast of the Snøhvit gas field (Figure 1) in the Norwegian sector of the Barents Sea. It is the first oil field in the Norwegian sector of the Barents Sea to be in production (March 2016). The majority of the NBS discoveries indicate a dominance of gas over oil. The oil reserves in the Snadd Formation of the Goliat field were not included in the Plan for Development and Operations (PDO). As a result, the Snadd Formation has not been the focus in earlier studies from a quantitative seismic petrofacies characterisation perspective.

However, a better understanding and delineation of the fluvial sand facies at the top of the Snadd Formation should provide additional insight into the porosity distribution for the cleanest sand intervals.

From a geophysical perspective, the Snadd Formation is challenging for the seismic lithology and fluid characterisation for three main reasons; i) relatively thin, silty-shaly sandstone units not ideal for AVA (Amplitude Versus Angle) analysis, ii) significant petrofacies overlap in rock physics elastic properties, and iii) overconsolidated reservoir due to uplift stiffens both the rock frame and pore space, thereby reducing the seismic fluid sensitivity. The main objective of this study is to discriminate and map out clean reservoir sands within the Snadd Formation using a multidisciplinary workflow combining spectral analysis, facies-based Bayesian inversion and supervised neural networks.

GEOLOGICAL SETTING

The Uralian mountain chain is one of the last collision elements close to the study area in Permian-Triassic times and represents an important source area for the dominantly siliciclastic sediments. Collapse and erosion of this orogeny, together with sediments from the basement rocks in the Kola peninsula, gradually filled the Barents Sea area mainly from the southeast (Mørk 1999; Glørstad-Clark et al., 2010; Henriksen et al., 2011b).

Structurally, the Troms-Finnmark Fault Complex (TFFC) is one of several regional faults in the area (Figure 1) and it cuts across the Goliat Field. The TFFC has a series of listric normal faults (Faleide et al., 1984; Gabrielsen, 1984; Gabrielsen et al., 1990; Mulrooney et al., 2017) forming a prominent roll-over anticline which provides structural closure for the field. Later Cenozoic uplift and exhumation in the Goliat area resulted in approximately 1000 to 1500 m of net erosion (Ohm et al.,2008; Henriksen et al., 2011b; Baig et al., 2016). This implies that the reservoirs have been exposed to much higher pressures and temperatures (i.e., more mechanical and chemical compaction) than at their present depths.

As mentioned earlier, the Snadd Formation is the main focus in this study (Figure 2a). The Barents Sea was part of a large and shallow inland sea, during the time when the Snadd Formation was deposited in the Late Ladinian to Early Norian (Dalland et al., 1988). According to Glørstad-Clark et al. (2010), the main depocenter during this time was located around present day Loppa High.

The regional sequence stratigraphic framework for the Snadd Formations has been documented by several authors (Glørstad-Clark et al., 2010; Klausen et al., 2015). The chronostratigraphic subdivision of the Snadd Formation is based on regionally correlated maximum flooding surfaces (MFS). The Top Snadd Formation sands in the Goliat field are capped by shales of the Fruholmen Formation. It represents the boundary between the Late Triassic Carnian and Norian Stages. This capping shale unit shows a characteristic higher acoustic impedance (AI) than the underlying Snadd Formation sands (Figure 2b). This results to a strong negative reflection coefficient. Note that positive amplitudes represent negative reflection coefficients in Figure 2b due to the reverse polarity of the data. The upper part of the Snadd Formation contains thicker and cleaner sands, as opposed to the middle section with more heterolithic or thin interbedded (“ratty”) sands and shales. The base of the Snadd Formation (Ladinian) overlying the Kobbe Formation is dominated by marine shales. This gross vertical change in the sand proportion can easily be seen by looking at the gamma ray log and sand flag (Figure 2b). The Snadd Formation has a southeast to northwest regional depositional dip (Riis et al., 2008; Glørstad-Clark et al., 2010; Klausen et al., 2015). The boundary between the Snadd Formation and the Kobbe Formation (Anisian to Early Ladinian) below, is characterized by a drop in AI from the basal anoxic shales of the Snadd Formation to the sand prone Kobbe Formation.

The systematic change in the depositional environments for the Snadd Formation, from open marine at the base to non-marine fluvial sediments at the top, translates into an increase in the net-to-gross (NTG) and quality of the reservoir sands towards the top of the formation. A north – south correlation profile through the available wells is shown in Figure 3a. The wells tops are flattened at the top Snadd Formation pick. Small-scale internal flooding surfaces can be seen bounding a series of stacked fining upward channel sands (blue arrows in the zoomed view in Figure 3a) based on the gamma ray log motif. The NTG at one of the deviated wells (Well-D) shows an anomalous proportion of sand within the Snadd Formation. The same outlier well is located structurally lower in a down – faulted segment compared to the other wells and is bounded by a relay-ramp fault system (Figure 3b).

DATABASE AND METHOD

Long-offset multi-azimuth (MAZ) 3D seismic, wireline logs, prestack depth-migrated (PSDM) velocities, and stratigraphic horizons were provided by the PL229 licence. The MAZ (127°, 67°, and 7°N) 3D seismic data over the Goliat Field each covers an area of approximately 209 km^2. During the processing of the seismic data (Buia et al., 2010), the partial angle stacks from the individual azimuths were rotated and referenced to 127°N (consistent with previous older survey azimuth). The near-angle (17°), mid-angle (32°), and far-angle (45°) partial stacks from each rotated azimuth are stacked to provide high quality angle stacks used as input in this study.

The well database consists of seven exploration and appraisal wells. Of these seven wells, two are not drilled through the entire Snadd Formation. Two of the remaining wells (oil- and brine-filled within the Snadd Formation) have been drilled through the entire formation, and in addition contain measured V_s logs. The relevant elastic logs of compressional velocity (V_p), shear velocity (V_s) and bulk density (Rho), alongside a suite of other formation evaluation logs (gamma ray, resistivity, porosity, etc.) have been used for petrofacies characterisation and discrimination during the feasibility analysis. A summary of the data-driven multidisciplinary method used to delineate clean sand units in the Snadd Formation is shown in Figure 4. The workflow can be subdivided into the following main steps:

1. End member depth trend analysis and stochastic forward modelling,
2. Rock physics feasibility and facies discrimination
3. Well –to – seismic ties and spectral decomposition for seismic geomorphology
4. Facies-based Bayesian inversion to predict absolute elastic properties and facies.
5. Supervised neural network for porosity estimation

End-member depth trends and stochastic forward modelling

A rock physics feasibility analysis is important in identifying the appropriate quantitative interpretation strategy for the different gross depositional environments within a given basin. This can be done using crossplots between various well log elastic properties and geological variables like porosity, volume of shale, and water saturation. The degree of facies separation in different elastic domains as a function of depth, provides clues as to which elastic parameters best discriminate the facies of interest. Siliciclastic sediments dominate the Triassic Snadd Formation.

As a result, end member sand and shale facies (Figure 5) have been picked in all the available wells spanning drilled depth. These end-member picks represent the cleanest example of a specific lithofacies. These picks are based on drilling reports, and the full suite of measured and computed petrophysical logs. For the clean sand end-member, the variation in pore fluid properties are also taken into account. The Backus average for each picked zone in the well is used as a single point in the end-member depth trend. During the manual picking process, the relative quality of each end-member pick is assessed from how close the individual pick histogram is to a normal distribution. This ensures that small unusual outliers are not considered and leads to more robust and representative end-member trends.

Once the representative depth trends are obtained for the in situ fluids, Gassmann (1951) fluid substitution is then applied (i.e., referencing all the fluid trends to brine) to effectively remove the scatter in the elastic property depth trends due to variations in the fluid type. The quartz grain and pore fluid properties used for fluid substituting the sand end-member trends are shown in Table 1. The effective porosity and saturation for each zone pick is obtained from the well logs. The dry rock bulk modulus is inverted for (using Gassmann's equation), given the moduli of quartz and porosity. As a result of a varying porosity input, the inverted dry rock bulk modulus also varies as a function of depth. The final brine-filled, end-member depth-dependent trends can then be used as input to construct i) depth varying stochastic Amplitude Versus Angle (AVA) forward models, ii) depth dependent Gaussian Probability Density Functions (PDFs) of the absolute elastic properties, and iii) the effective Extended Elastic Impedance (EEI) rotation angles (Whitcombe et al., 2002) for lithology and fluid stacks at different depths of investigation.

The stochastic forward models (Figure 6) are based on random sampling from the PDFs at the target depth, between a specified lithology and fluid composite (litho-fluid) across an interface.

This stochastic forward modelling analysis goes beyond the end-member brine trends, but can also include desired or expected litho-fluid composites at different depths. These trends are important in understanding the key elastic parameters controlling the facies discrimination as a function of depth. The depth varying PDFs can later be used to classify the inverted volumes, or other prestack data cross plot combinations (i.e., AVA intercept and gradient, near- versus far-angle stacks), to the desired facies of interest.

These end-member depth trends may be utilised directly in building the very important low-frequency model (LFM) required to obtain absolute elastic properties from a model-based inversion. This requires good prior knowledge of the NTG, which is then used to specify the representative proportions of the end-member trends within each stratigraphic interval. The challenge in doing so is that the NTG distribution within the Snadd Formation is the main objective of the study and the reason for inverting in the first place. As a result, we adopt a different approach to obtain the required low-frequency model, which is explained in the facies-based simultaneous inversion section of the workflow. Prior to the facies-aware inversion, we need to define the target petrofacies from available well data and assign depth dependent rock physics trends.

Petrofacies classification and per-facies depth trend analysis

Rock physics crossplots such as AI versus V_p/V_s ratio, colour coded with shale volume and porosity (Figure 7a and Figure 7b respectively), have the potential to reveal facies clusters or trends in petroelastic space. Deciding on the number of petrofacies to invert for is not always trivial. There is a trade-off between the number of different petrofacies needed for subsurface characterisation and the resolution limitations (i.e., narrow bandwidth compared to well log data) of the seismic.

A binary petrofacies log has been created using effective porosity (PHIE) cut-off (PHIE < 12% represent non-reservoir) to distinguish reservoir from non-reservoir. This cut-off is based on how well the derived facies classes separate in the elastic domain. The corresponding AI versus V_p/V_s PDFs of the binary facies are shown in Figure 7b. This binary log was subsequently upscaled based on filtering the PHIE log using a Gaussian function over a 15-m window, and subsequently applying the same cut-off. The upscaled log is used at a later stage for comparison to the inversion-derived facies log at the well locations. Meanwhile, the unscaled facies log is used to define per facies rock physics depth trends. Figure 8a shows the depth trends (using only five vertical wells) for reservoir sand and non-reservoir facies within the Snadd and Kobbe formations interval. Two deviated wells were left out of the depth trend analysis. One of these wells is used as a quality control (QC) blind well for the inversion and neural network predictions. The depth trend analysis provides, i) the prior facies proportions for subsequent facies-based Bayesian inversion, ii) uncertainty distribution (dotted line in Figure 8a) in the elastic properties per facies with depth, and iii), per-facies rock physics cross correlations (Figure 8b) between V_p, V_s, and Rho. The prior probabilities obtained from the depth trends are used as initial estimates only and are adjusted down slightly to account for bias in well placement (since available wells target areas with expected high NTG). The uncertainty distribution of the elastic properties with depth and the corresponding cross correlations provide important facies-dependent constraints during the Bayesian facies-aware simultaneous inversion process.

Well-to-seismic ties and spectral analysis

Well ties represent a crucial step in understanding the relationship between the seismic amplitudes and the impedance contrasts at the wells. This requires a comparison between a synthetic seismic trace and the seismic trace at the well location. The convolutional forward model needed to create the synthetic trace requires a wavelet. This wavelet can either be derived statistically without using the wells (assuming the seismic data is zero phase), or using a deterministic approach using wells (no assumption of the phase of the data). For this work, we have used the White (1980) method to estimate the wavelets shown in Figure 9a. This deterministic method provides the appropriate wavelet scaler required to link the reflection coefficients computed at the wells to the corresponding observed seismic amplitude. The elastic logs (V_p, V_s, and Rho) are Backus averaged to the seismic bandwidth prior to convolving with the derived wavelet. The quality of the tie is quantitatively assessed using attributes such as the Proportion of Energy Predicted (PEP) and the cross correlation coefficient. The Root Mean Square (RMS) error of the wavelet obtained for each angle stack is used during the inversion to weight the contribution of the near-, mid-, and far-angle stacks differently. The signal-to-noise (SNR) at the target is estimated from the PEP following,

$$SNR = \sqrt{\frac{PEP}{1-PEP}} \tag{1}$$

A spectral decomposition is then carried out on the full stack data. This decomposes the seismic traces to user defined constituent frequencies through a Fourier transform operation within the target window for the Snadd Formation. Analysis of the resulting amplitude spectrum (Figure 9b) and the frequency cube over sand rich intervals around the wells provide insight into which frequencies to select for a Red – Green – Blue (RGB) frequency blend. Seismic geomorphologic features of interest are subsequently highlighted based on an RGB flattened horizon slice for the top Snadd Formation.

Facies-based simultaneous Bayesian inversion

Seismic data is well known to be bandlimited. However, the low-frequency component of the seismic data is more crucial to the successful application of absolute seismic inversion schemes (Cooke and Schneider, 1983). These low frequencies contain the subtle compaction trends, which, if not properly captured, will result in erroneous estimates of the absolute elastic properties, irrespective of the optimisation inversion algorithm used.

Several practitioners over the years have used different methods to obtain this crucial low-frequency component of the earth. One method is to apply a high-cut frequency to horizon guided interpolations of well log elastic properties. The quality of the LFM is dependent on the number and spacing of the wells. Other methods use seismic velocities (stacking or PSDM velocities), either as a standalone input, or co-krigged with the well logs (Yenwongfai et al., 2017a). The seismic Rho and Vs LFMs can be subsequently obtained by applying rock physics transforms such as the Gardner et al. (1974) and Castagna et al. (1998) equations, respectively. The pitfall in using seismic velocities alone is that the corresponding LFMs for Vs and Rho do not contain any independent information. Therefore, in geologic scenarios where the primary facies discriminating parameter is V_p/V_s ratio, the inversion for the purpose of facies discrimination is compromised before one begins. Another method could be to use facies dependent end-member trends as input. The challenge here, as mentioned earlier, is in specifying the correct proportion of the end members, for each zone of interest, to obtain one average LFM. However, it is beyond the scope of this paper to discuss the pitfalls in constructing the LFM or a review of different inversion methods. We refer the reader to Sams and Carter (2017) for more details and alternative methods for constructing a LFM. In addition to the challenges in constructing a LFM, classical inversion algorithms treat the problem as only continuous (impedances), and ignoring facies (discrete) which together drive the seismic response.

In order to overcome these limitations, Kemper and Gunning (2014) introduced a novel approach where the impedances and facies are jointly inverted for in a Bayesian framework. The same method was applied in this study. Here, the LFM is an output (constructed during the inversion) and not an input. Facies-dependent depth trends for V_p, V_s, and Rho are used to construct two LFM representatives for reservoir sand and non-reservoir facies in the Snadd Formation. This ensures that the compaction trends and the associated uncertainty with depth is accounted for per facies. For a detailed review on the inversion scheme, we refer the reader to Kemper and Gunning (2014).

Once facies are obtained, inverse rock physics models per facies (Johansen et al., 2013) can be applied to the inverted facies result to obtain petrophysical parameters like shale volume (Vsh), PHIE, and water saturation. For good results, core data calibration is often required. In the absence of available core data, multi-attribute analysis and neural networks were used to combine all available data into one analysis and search for non-linear trends in the data.

Supervised neural network

Neural networks have the advantage of exploiting complex non-linear relationships between multiple input parameters to predict a target output. Step-wise linear regression based algorithms might miss some important non-linear information vital for reservoir properties such as PHIE. Utilising neural networks or multi-attribute seismic analysis for lithology characterisation is not new (e.g., Hampson et al., 2001; Pramanik et al., 2004). However, there has been an increasing trend in integrating seismic inversion products with machine learning algorithms to squeeze out more subsurface information.

The main objective of the supervised neural network in this study is to put together in one analysis all relevant attributes derived from the inversion which are indirectly related to the pore volume.

A three-layer feedforward network has been used with a total of 15 nodes in the hidden layer. A sigmoid activation function has been used. The training process is done in time and requires a seismic consistent sampling rate (4 ms in our case) for the target porosity logs (computed from logs measured in depth). Good seismic–to–well ties are crucial during the training phase. First, single attributes are compared and ranked based on their correlation with the PHIE log at the training wells. Then, several multi-attribute combinations are compared and ranked according to the training and validation errors. The optimum number of attributes are chosen based on the validation error profile associated with the successive addition of attributes to the training process. This step tries to reduce the risk of over classifying the attributes in the final neural network. This optimum attribute set is then used as input to the multi-layer feed-forward neural network (MLFN). Optimisation of the cost function is achieved through a combination of conjugate gradient and simultaneous annealing algorithms to search for the global minimum. Meanwhile the optimum synaptic weights between the nodes are derived during the training, by backpropagation of the error in the predicted log when compared to the actual porosity log. The final extracted clean sand geobodies are based on PHIEs > 15 % within the reservoir sand predictions obtained from the facies-based inversion.

RESULTS AND DISCUSSION

Figure 5 shows Gassmann corrected end-member depth trends for sand and shale. All the trends are referenced to brine and plotted from the mudline. The dotted lines represent two standard deviations from the mean trend (solid lines). The black circle on the depth trends represent the approximate top Snadd Formation. As expected, both V_p trends for sand and shale increase as a function of depth due to increasing mechanical (stress dependent) and chemical (temperature and time dependent) compaction with burial. The porosity loss with increasing burial depth is also captured in the inverse relationship between V_p and PHIE. The end-member trends for P-impedance and Poisson's ratio (ν) become more unique at burial depths greater than that represented by the Snadd Formation. The V_p – Rho relationship is more unique (better end-member separation) than the V_p – V_s trend.

The stochastic forward modelling results for different fluid scenarios using the end-member depth trends as input are shown in Figure 6. The impact of compaction with increasing burial depth on fluid discrimination is illustrated using the Gaussian ellipses and 1D PDFs for AI and V_p/V_s ratio. Gaussian models are compared for brine, oil, and gas-filled sands with a 75% NTG. The centre of each Gaussian ellipse represents the mean for the class. The distance from the mean to the edge of the ellipse is equivalent to two standard deviations. At both modelled depths (1000 m and 2000 m TVD ML), there is a significant overlap of the different fluid scenarios. The V_p/V_s ratio shows better discrimination compared to AI at both depth intervals. With increasing burial depth (i.e., at 2000 m TVD ML), we observe that the ellipses for the different fluid scenarios overlap much more. This is as expected because the rock framework becomes stiffer and it is more challenging to determine the pore fluid content. Such an analysis should be done for target reservoirs with contrasting burial depths such as the Snadd Formation, in order to determine the best set of elastic parameters to be used for interpretation at different depths of investigation. For very heterolithic formations with multimodal facies characteristics, the Gaussian assumption might be inadequate and non-parametric multivariate PDFs derived from point density contours in elastic space are more appropriate.

Figure 10 shows the RGB spectral blending flattened top Snadd Formation using iso-frequencies (11, 25, and 55 Hz for Red, Green, and Blue, respectively) decomposed from the full stack data through a Fourier transform operation. These frequencies were selected based on the dominant frequency and slope changes in the amplitude spectrum. The dominant frequency from the spectral analysis is ~ 25 Hz. Some large – scale trends can be observed with the hot colours on the map. These bright yellow-red trends are interpreted to represent higher NTG intervals after comparing with the lateral NTG observed at the wells. A strong anomaly around Well-D corresponds with the anomalous sand proportion within the top of the Snadd Formation in the relay ramp area (Figure 3a). Most of the large – scale trends in the northern part of the study area have a NNE orientation (marked with dotted blue lines in Figure 11), except around Well-D with an almost E-W trend. Meanwhile in the southwestern part of the study area the dominant trend changes to ENE. The regional progradation of sediments from the Polar Urals was oriented SE-NW, but some local variations may have occurred around the study area in the Southern Hammerfest Basin (Glørstad-Clark et al., 2010; Klausen et al., 2014). Meanwhile, the E-W trends likely correspond with a locally sourced trend. The branching points along the TFFC (indicated with arrows in Figure 10) show some strong red anomalies with geometries consistent with point-sourced lobes where this major fault branches. The E-W trends and the anomalies tied to the TFFC might be indications of minor local Late Triassic tectonic activity along this master fault (Mulrooney et al., 2017). However, the fidelity of the flattening process is questionable in areas with dense faulting, which limits the resolution of the extracted anomalies, especially when dealing with very thin sands. A closer look into the details in a fault segment with less structuring reveals finer details of what we interpret to be a meandering channel, with a point bar complex. The width of these point bar complexes approximately range between 200 – 250 m. In a low NTG environment distal from the main source area, it is expected that the channels will develop mud-rich and stable levees, which help in confining the channel and therefore limiting the avulsion frequency. A schematic representation of the meander channel and point bar complex is also shown in Figure 11.

From a qualitative point of view, the seismic-to-well tie within the Snadd Formation is higher at the top and base of the formation. However, it is important to quantitatively assess the fit by examining the PEP and cross correlation over the interval of interest. In the example shown within Track 9 in Figure 12, the PEP is 78 % and the cross correlation is 88 % thus representing a good fit over the target zone.

Figure 11 also shows the comparison between the well logs and the results from both the facies – based Bayesian inversion and the neural network PHIE prediction at the reference well. The well log curves are shown in black, the predicted logs in red, and the blocky red logs within the same track represent the combined facies LFM output. There is a fairly good match between the inverted logs and the actual logs, especially for the thicker sand intervals. In contrast to a model-based deterministic inversion (with the LFM constructed from structurally guided well interpolation), the QC is not compromised because the LFM is not supplied but computed during the inversion. The difference (i.e., residuals) between the inverted traces and the actual seismic trace are also shown in Track 12 in Figure 11 for visual comparison.

The limitations in the seismic bandwidth and the effects of upscaling are more apparent when comparing the derived facies model (Track 7) to the unscaled (Track 5) and upscaled well log facies (Track 6) presented in Figure 11. In this example, there is a good match in the predicted sand units approximately ≥ 15 m. The prior probability for reservoir sand and non-reservoir (Track 8) within the upper part of the Snadd Formation was set as equal. Some smoothing was applied to the prior probabilities (seen as a step pattern on the prior probability curves) to account for gradational facies changes. In addition, the prior probability for reservoir sand is set to decrease towards the base of the Snadd Formation; this is consistent with geologic prior information about the vertical NTG distribution in the available wells. As expected, sand units smaller than 10 m are hardly present in the upscaled facies log and are equally not detected in the inverted facies model. The final facies result is the maximum a posteriori (MAP) facies or most likely facies. In this binary system (reservoir and non-reservoir), this implies a facies probability greater than 50%. However, if more than two facies are being inverted for, it is important to remember that the MAP facies in the Bayesian classification could have a probability as low as 34%.

Figure 12a shows the training (black curve) and validation error (red curve) profiles for a multi-attribute analysis performed to determine the optimum set of attributes to use further in the neural network. Table 2 contains the final list of 10 attribute transforms used. The combined shear Impedance (SI) LFM from the inversion showed the best individual correlation to PHIE. A well-known problem for neural networks is the potential to over classify the training data set. One way to address this challenge is to start the analysis with a multi-attribute set that results in the smallest validation error (i.e., the lowest turn around point in the validation error profile). The average training error for all wells decreases with successive addition of attributes to the analysis. The lowest minima in the validation error profile occurs at the 10th attribute transform. Each data point on the validation error is obtained leaving out a target well in the analysis and using the other wells to predict the desired property. If more than 10 attributes are used, the prediction quality starts to decrease and we start over classifying the data, i.e., the point at which the average well training error keeps reducing while the validation error progressively increases.

Figure 12b shows a cross plot between the neural network predicted PHIE and actual PHIE log for five wells. The cross correlation between them is 0.67. This plot highlights the underlying challenge in predicting thin, below-resolution clean sand intervals. This challenge is common to the inversion and the neural network result. The prediction does not fully capture the upside in the PHIE estimates. No predicted PHIE data points are observed above 0.2. This is partly due to the sampling rate (4 ms) used in the training which is rather coarse (i.e., for thin high PHIE sand intervals within the Snadd Formation), but consistent to the seismic sampling rate. Track 4 in Figure 11 shows the comparison between the neural network predicted log (red) and the well log (black). The predicted log fully captures the PHIE trend in the log, and is consistent with the inverted facies (Track 7) at the well location.

An arbitrary line (Figure 13) through the reference well and a blind deviated well (i.e., well neither used in the depth trend for the inversion nor in the training for PHIE) validates the inversion and neural network results away from well control. In Figure 13a, the low AI layers correlate well to reservoir sand facies (Figure 13b) with relatively higher PHIE (Figure 13c) within the upper part of the Snadd Formation. The quality of the facies prediction can be quantified using a confusion matrix. The off-diagonal elements in the matrix indicate the degree of error. The confusion matrices for both wells are displayed in Figure 13b below the corresponding well. For the reference well, the facies aware inversion correctly classifies the reservoir facies of interest 87.5 % of the time and wrongly classifies it as non-reservoir 12.5 % of the time. The facies prediction for the deviated blind well, which was not included in defining the facies depth trends, is also shown. The reservoir sand prediction success is 65.38 %. This well has thinner sand units compared to the reference well, and this could be one reason for a lower classification success. In reservoirs where the facies do not show separate clusters in a rock physics space, the wavelet scaling becomes more crucial to the inversion result. However, the White (1980) method provided the appropriate wavelet scaling required in our case. Notice that the middle to lower section of the Snadd Formation (Figure 13c) is dominated by PHIEs < 0.1 and is correctly classified as non-reservoir (Figure 13b) in the facies-based inversion. Despite the upside limitation in the predicted PHIE result, it is still very useful in a qualitative sense when combined with the inverted facies, to highlight the cleanest intervals within the predicted reservoir sands in the upper parts of the Snadd Formation.

Figure 14 shows a horizon slice for PHIE and facies at the top of the Snadd Formation interval. The ovals and arrows from the RGB flattened slice in Figure 10 are shown for a visual qualitative comparison between the attributes. The extent of the anomalies indicating gross depositional trends (Figure 10) are much larger than observed in the PHIE (Figure 14a) and Facies (Figure 14b) horizon slices. In general, there is consistency between the PHIE and Facies horizon slices with a few exceptions. The large white ovals in Figure 14 show areas with predicted reservoir sand but with very low porosity predictions. This could be interpreted to represent more cemented sands, as this area structurally lower (easily seen in Figure 3b around the grey arrow) within a graben structure bounded by relay ramp faults. The combined map (Figure 14c) showing the clean sand geobodies represent predicted sand facies with PHIEs > 15 %. Artefacts are produced along the faults in both the facies and PHIE maps and reliability of the maps increase away from the faults.

CONCLUSION

Properly constrained facies-dependent rock physics depth trends are very important for successful quantitative seismic reservoir characterisation within the Snadd Formation in the Goliat field.

However, if these trends are to be used in other parts of the SW Barents Shelf, an appropriate reference depth needs to be thoroughly investigated before hanging the depth trends in areas with seismic data but no wells. Fluid sensitivity is shown to decrease with depth based on the PDFs obtained from the end member trends. Spectral decomposition and RGB blended results reveal two main depositional trends: i) a NNE trend compared to the SE – NW regional clinoform progradation of sediments from the Uralide orogeny, and ii) an E-W local trend which likely represents local sources tied to pulses of sediments at branching points of the TFFC. The Snadd Formation is strongly compartmentalised so the fidelity of the flattened slice is uncertain in intensively faulted areas.

Despite the considerable overlap of the binary facies in a rock physics elastic space, the facies-aware Bayesian inversion is still able to largely discriminate reservoir sands from non-reservoir at a blind well (i.e., not used in the depth trend analysis). When inverting for more than two facies, it is crucial to further investigate the probability of the most likely facies which can be as low as 26% (i.e., if four facies are inverted for).

The neural network porosity predictions capture the general vertical trends in the wells, but do not properly capture the very thin high PHIE sands. However, the PHIE results are consistent with the inverted facies and can be used in a qualitative manner to discriminate the best reservoir facies with high PHIE. Areas interpreted to represent point sources for sediment input along the TFFC from the RGB flattened slice are supported by both facies and PHIE predictions. Neural networks should be viewed as an additional tool to decode complex relationships in the data especially when available linear and non-linear rock physics models fail.

Acknowledgements

This work is partly funded by the project “Reconstructing the Triassic Northern Barents shelf; basin infill patterns controlled by gentle sags and faults” (Trias North) under grant 234152 from the Research Council of Norway and with financial support from Tullow Oil Norge, Lundin Norway, Statoil ASA, Edison Norge and Dea Norge. We thank Eni Norge and Statoil ASA of the PL229 license for permission to publish the data, and Filippos Tsikalas (Eni Norge) for valuable discussions. This work has been carried out using RokDoc, HampsonRussell, and DUG Insight commercial software packages at the University of Oslo (UiO).

REFERENCES

Aki, K., and P. G. Richards, 1980, Quantitative seismology: Theory and methods: Freeman and Co.

Baig, I., Faleide, J. I., Jahren, J., and Mondol N. H., 2016, Cenozoic exhumation on the southwestern Barents Shelf: Estimates and uncertainties constrained from compaction and thermal maturity analyses. Marine and Petroleum Geology. ISSN 0264-8172. 73, s 105-130. doi: 10.1016/j.marpetgeo.2016.02.024

Buia, M., C. Cirone, J. Leutscher, S. Tarran, and B. Webb, 2010, Multi-azimuth 3D survey in the Barents Sea: First Break, 28, 65–69.

Castagna, J. P., H. W. Swan, and D. J. Foster, 1998, Framework for AVO gradient and intercept interpretation: Geophysics, 63, no. 3, 948–956, http://dx.doi.org/10.1190/1.1444406.

Cooke, D. A., and W. A. Schneider, 1983, Generalized linear inversion of reflection seismic data: Geophysics, 48, 665–676, doi: 10.1190/1.1441497.

Dalland, A., Worsley, D., Ofstad, K., 1988. A Lithostratigraphic Scheme for the Mesozoic and Cenozoic Succession Offshore Mid- and Northern Norway. Direktoratet, Stavanger.

Faleide, J. I., S. T. Gudlaugsson, and G. Jacquart, 1984, Evolution of the western Barents Sea: Marine and Petroleum Geology, 1, 123–150, IN1–IN4, 129–136, IN5–IN8, 137–150, doi: 10.1016/0264-8172(84)90082-5.

Gabrielsen, R.H.,1984, Long-lived fault zones and their influence on the tectonic development of the southwestern Barents Sea. Journal of Geological Society of London, 141, 651-662.

Gabrielsen, R.H., Færseth, R.B., Jensen, L.N., Kalheim, J.E. & Riis, F., 1990, Structural elements of the Norwegian Continental Shelf. Part I: The Barents Sea Region. Norwegian Petroleum Directorate Bulletin, 6, 33.

Gardner, G. H. F., L. W. Gardner, and A. R. Gregory, 1974, Formation velocity and density — The diagnostic basics for stratigraphic traps: Geophysics, 39, no. 6, 770–780, http://dx.doi.org/10.1190/1.1440465.

Gassmann, F., 1951, Elastic waves through a packing of spheres: Geophysics, 16, 673–685, doi: 10.1190/1.1437718.

Glørstad-Clark, E., J. I. Faleide, B. A. Lundschien, and J. P. Nystuen, 2010, Triassic seismic sequence stratigraphy and paleogeography of the western Barents Sea area: Marine and Petroleum Geology, 27, 1448–1475, doi: 10.1016/j.marpetgeo.2010.02.008.

Hampson, D. P., J. S. Schuelke, and J. A. Quirein, 2001, Use of multiattribute transforms to predict log properties from seismic data: Geophysics, 66, 220–236, doi: 10.1190/1.1444899.

Henriksen, E., A. E. Ryseth, G. B. Larssen, T. Heide, K. Rønning, K. Sollid, and A. V. Stoupakova, 2011b, Tectonostratigraphy of the greater Barents Sea: Implications for petroleum systems: Geological Society, London, Memoirs 35, 163–195.

Johansen, T. A., E. H. Jensen, G. Mavko, and J. Dvorkin, 2013, Inverse rock physics modeling for reservoir quality prediction: Geophysics, 78, no. 2, M1–M18, doi: 10.1190/geo2012-0215.1

Mørk, M. B. E., 1999, Compositional variations and provenance of Triassic sandstones from the Barents Shelf: Journal of Sedimentary Research, 69, 690–710, doi:10.2110/jsr.69.690.

Mulrooney, M.J., Leutscher, J., and Braathen, A., 2017, A 3D structural analysis of the Goliat field, Barents Sea, Norway. Marine and Petroleum Geology, 86, 192-212.

Ohm, S. E., D. A Karlsen, and T. J. F. Austin, 2008, Geochemically driven exploration models in uplifted areas: Examples from the Norwegian Barents Sea: AAPG Bulletin, 92, 1191–1223, doi: 10.1306/06180808028.

Kemper, M., and J. Gunning, 2014, Joint impedance and facies inversion — Seismic inversion redefined: First Break, 32, 89–95.

Klausen, T.G., Ryseth, A.E., Helland-Hansen, W., Gawthorpe, R., Laursen, I., 2014, Spatial and temporal changes in geometries of fluvial channel bodies from the Triassic Snadd Formation of offshore Norway. J. Sediment. Res. 84, 567e585.

Klausen, T. G., Ryseth, A. E., Helland-Hansen, W., Gawthorpe, N., Laursen, I., 2015, Regional development and sequence stratigraphy of the Middle to Late Triassic Snadd Formation, Norwegian Barents Sea: Marine and Petroleum Geology, 62, 102-122, doi.org/10.1016/j.marpetgeo.2015.02.004.

Pramanik, A. G., V. Singh, R. Vig, A. K. Srivastava, and D. N.Tiwary, 2004, Estimation of effective porosity using geostatistics and multiattribute transforms: A case study: Geophysics, 69, 352–372, doi: 10.1190/1.1707054.

Riis, F., B. A. Lundschien, T. Hoy, A. Mork, and M. B. E. Mork, 2008, Evolution of the Triassic shelf in the northern Barents Sea region: Polar Research, 27, 318–338, doi: 10.1111/j.1751-8369.2008.00086.x.

Sams, M., and Carter, D., 2017, Stuck between a rock and a reflection: A tutorial on low-frequency models for seismic inversion, Interpretation, 5(2), B17-B27.https://doi.org/10.1190/INT-2016-0150.1

Whitcombe, D. N., P. A. Connolly, R. L. Reagan, and T. C. Redshaw, 2002, Extended elastic impedance for fluid and lithology prediction: Geophysics, 67, 63–67, doi:10.1190/1.1451337.

White, R.E. [1980] Partial coherence matching of synthetic seismograms with seismic traces. Geophysical Prospecting, 28(3), 333-358.

Yenwongfai, H. D., N. H. Mondol, J. I. Faleide, and I. Lecomte, 2017a, Prestack simultaneous inversion to predict lithology and pore fluid in the Realgrunnen Subgroup of the Goliat

Field, southwestern Barents Sea: Interpretation, 5, no. 2, SE75–SE96, http://dx.doi.org/10.1190/INT-2016-0109.1.

LIST OF FIGURES

Figure 1 Location map for the Goliat Field (adapted from NPD factmaps) in the Norwegian sector of the Barents Sea. The field is cut by the Troms-Finnmark Fault Complex within blocks 7122/7 and 7122/8 (Yenwongfai et al.,2017a)

Figure 2 Triassic chronostratigraphic framework comparison (a) for different authors. The subdivisions are based on 2nd and 3rd order sequences (Klausen et al., 2015). The Snadd Formation (target in this study) is also starred. The vertical change in the net-to-gross (as seen from the Sand Flag log track) effectively divides the interval into three main lithological zones (b). Zone 1 has thicker more consistent sand units. Meanwhile zone 2 and 3 have heterolithic sands and shales respectively. Maximum flooding surfaces (MFSs) bounding the top and base of the Snadd Formation are also indicated. The P-impedance log is superimposed on the full stack seismic section. Note that positive amplitudes on the seismic represent soft events.

Figure 3 Well correlation profile from north to south. Well-D has an anomalous high sand proportion within the Snadd Formation and is located within a relay ramp structure (black arrow). Well-D is a side track from Well-G (not visible in Figure 3b) and deviates further away from Well-G below the top Snadd Formation horizon. Minor faults around both wells might explain differences in the observed NTG. Gamma log motifs from Well-B show good examples of stacked fining upward channels bounded by flooding surfaces.

Figure 4 Workflow implemented for petrofacies and PHIE characterisation within the Snadd Formation. Depth trends play a central role in the feasibility study and during the inversion. The flow diagram shows the routes to clean sand delineation. The five main steps in the seismic reservoir characterisation workflow are highlighted in green.

Figure 5: End-member depth trends for sand and shale through the whole well interval. The Vp, Vs, Rho, and PHIE trends are the primary trends (a) while the other trends (b) are derived from the primary trends. The sand-end member trends have been Gassmann fluid substituted to brine. The black circle shows the approximate depth location of the top Snadd Formation.

Figure 6: Depth varying PDFs (a) based on stochastic forward modelling of the end-member trends (shown in Figure 5). The plots show the fluid discrimination of AI and Vp/Vs attributes as a function of depth. Sensitivity decreases with depth as shown by increasing overlap of each ellipse and PDFs. Also the effective extended elastic impedance (EEI) chi angle (c) using the depth trends are also shown. The black and red arrows indicate the effective lithology and fluid angles.

Figure 7 AI versus Vp/Vs cross plots colour coded with Vsh (a) and PHIE (b). The contour density for sand and shale are based on a PHIE cut-off using 12% as the threshold. Sands dominate at low AI and Vp/Vs ratios. However, the histograms still show a significant overlap of both facies.

Figure 8 Reservoir and non-reservoir depth trends within the Snadd and kobbe Formation time interval. These depth trends (a) provide the uncertainty distribution (standard deviation of the derived trend curve) of the elastic properties as a function of depth as well as the cross correlation and constraints between the elastic parameters per facies. A cross plot comparison (b) between the prior model derived from the depth trends and the corresponding well data are also shown.

Figure 9 Wavelet processing and spectral analysis. The near, mid, and far angle stack wavelets (a) have all been extracted using the White (1980) method. The wavelets have been extracted based on the offset location with the highest PEP close to the well bore. The signal and noise spectra (b) at the top of the Snadd Formation interval are also shown with the selected frequencies used in the RGB blend.

Figure 10: Spectral decomposition and RGB blending of selected frequencies displayed at the top Snadd Formation flattened horizon slice. The corresponding frequency spectra (Figure 9b) is also inserted for reference to the frequencies. The bright red arrows show a dominant NNE trend. Meanwhile close to the branching points along the Troms-Finnmark Fault Complex (TFFC), observed anomalies are oriented E – W (black dotted lines). The white dotted lines, show the anomaly around Well-D (anomalous sand proportion in Figure 3) indicated with a blue arrow. A detailed view around Well-E shows a schematic representation of a channel and point bar complex. Note that Well-E just sits at the edge of this anomaly.

Figure 11: Facies-aware inversion and neural network results at the reference well. The inverted elastic logs (blue logs in Track 2 and 3) are plotted alongside the LFM (low frequency model) output logs (red logs) in the same tracks. There is a good match between the inverted facies log (Track 7) compared to the upscaled (Track 6). The inversion synthetic logs and the residuals are also shown in Track 11 and Track 12. The predicted PHIE log (red) from the neural network shows a match to the thicker and better developed reservoir sands (above 1240 ms TWT).

Figure 12 Multi-attribute neural network training (a) and prediction correlation (b). The validation error is shown to increase after the 10th attribute transform in the multi-attribute analysis. Attribute number 1 – 10 are used in the neural network prediction. We refer the reader to Table 2 for more details in Figure 12a.

Figure 13 Arbitrary line section through the reference well (Well-A) and the blind well (Well-C). The simultaneous Bayesian Joint Impedance (a) and Facies (b) inversion results are compared with the neural network PHIE predictions (c). Good PHIEs observed at the upper part of the Snadd Formation (results from the neural network) are consistent with the predicted reservoir sands from the inversion. The quality of the facies predictions are illustrated in a confusions matrix below the respective wells. Diagonal elements in the matrix indicate the degree of success of the classification.

Figure 14 Horizon slices at the top of the Snadd Formation for effective porosity (a) and binary facies (b) over a 30ms window. The binary facies map is the result from the facies-based inversion, while the the porosity map is the output from the multi-layer feedforward neural network. The clean sand geobodies (c) represent predicted reservoir sand facies with PHIE greater than 15 %. Reservoir delineation is improved by qualitatively combining areas with good effective porosity in regions where reservoir sand is predicted by the inversion. The arrows and ovals from the flattened RGB slice in Figure 10, are inserted for visual comparison.

LIST OF TABLES

Table 1: Grain and fluid properties used as input for brine substitution of the sand end-member trend through Gassmann's equation. Quartz properties have been used for sand end-member grain properties.

Table 2: Multi-attribute transform list used as input to the neural network. Attribute numbers correspond to numbers used in Figure 13a. The attribute transform with the highest individual correlation to PHIE, is the Shear Impedance (SI) LFM output constructed during the inversion. Note that the errors associated with each successive is attribute is cumulative by applying all preceding attributes.

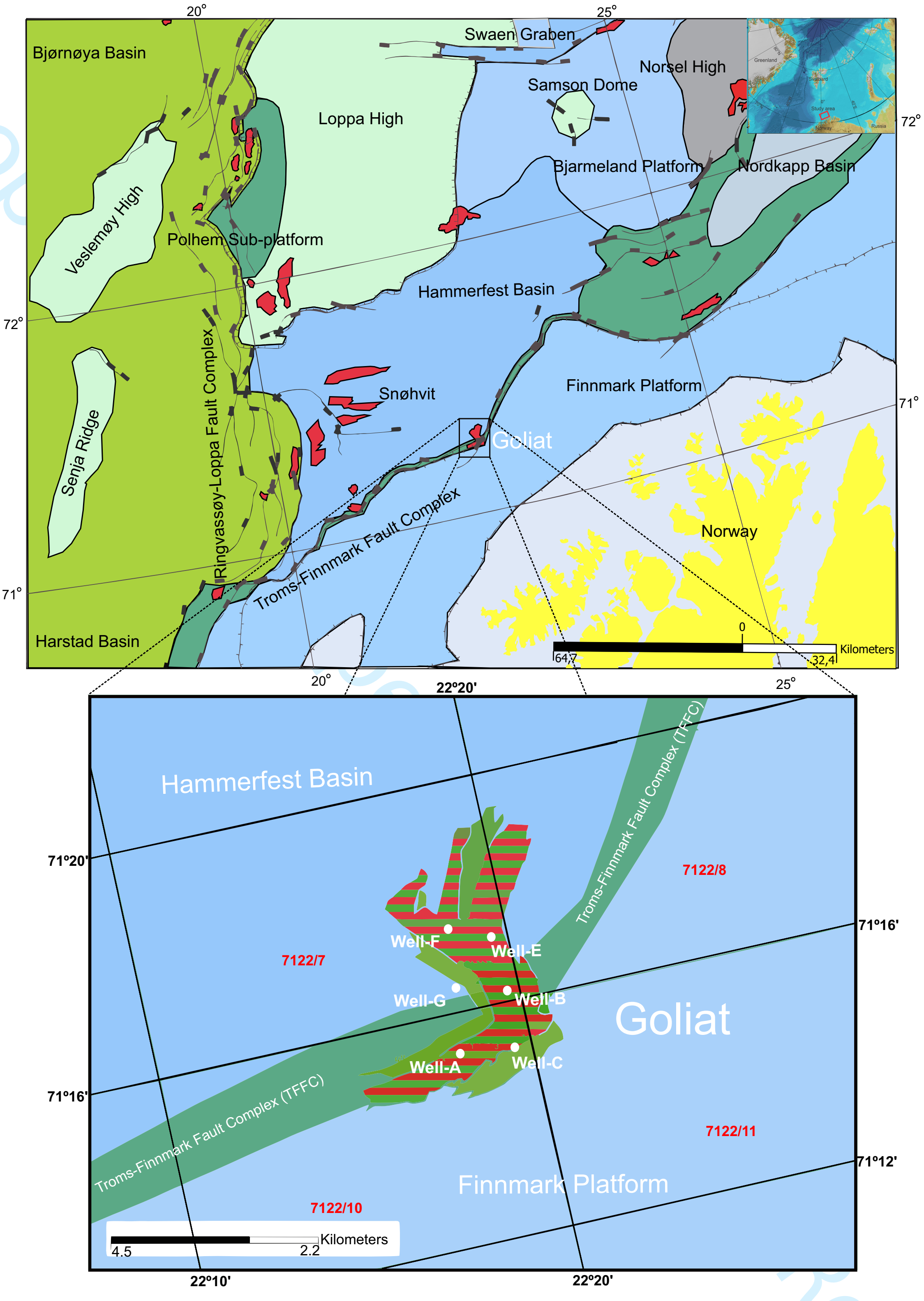

Figure 1 Location map for the Goliat Field (modified from NPD factmaps) in the Norwegian sector of the Barents Sea. The field is cut by the Troms-Finnmark Fault Complex within blocks 7122/7 and 7122/8 (Yenwongfai et al.,2017a)

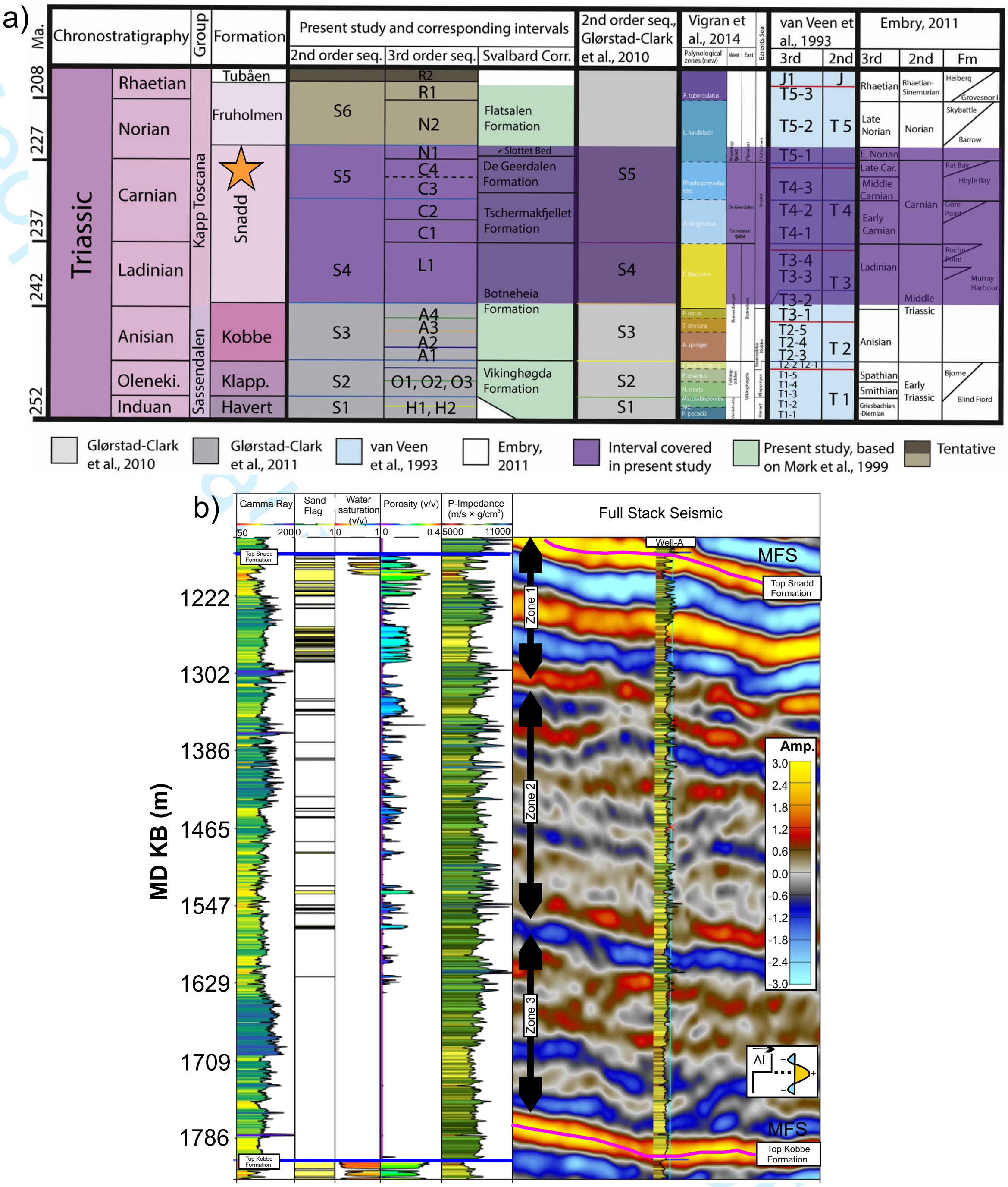

Figure 2 Triassic chronostratigraphic framework comparison (a) for different authors. The subdivisions are based on 2nd and 3rd order sequences (Klausen et al., 2015). The Snadd Formation (target in this study) is also starred. The vertical change in the net-to-gross (as seen from the Sand Flag log track) effectively divides the interval into three main lithological zones (b). Zone 1 has thicker more consistent sand units. Meanwhile zone 2 and 3 have heterolithic sands and shales respectively. Maximum flooding surfaces (MFSs) bounding the top and base of the Snadd Formation are also indicated. The P-impedance log is superimposed on the full stack seismic section. Note that positive amplitudes on the seismic represent soft events.

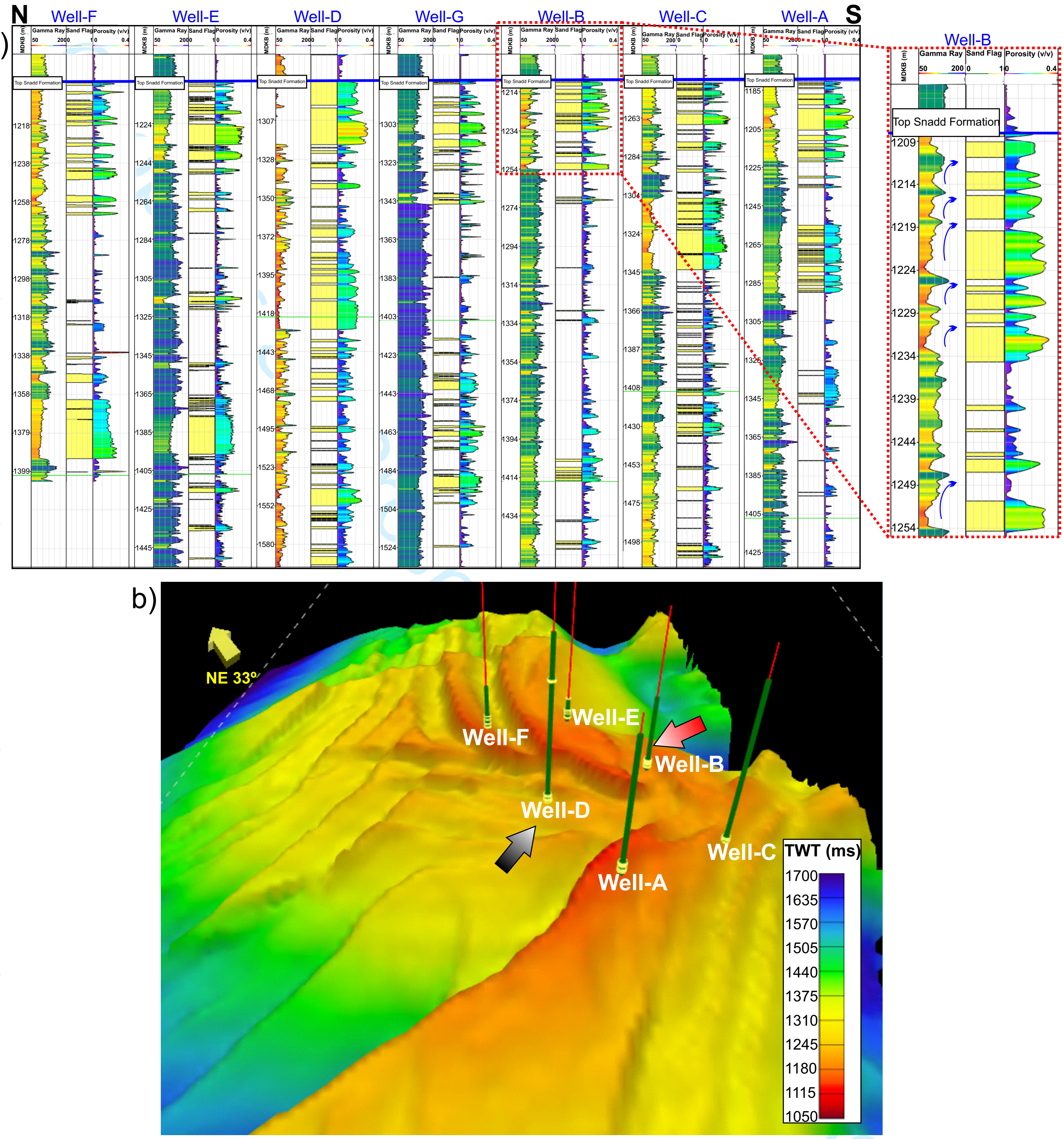

3D time structure map with available wells

Figure 3 Well correlation profile from north to south. Well-D has an anomalous high sand proportion within the Snadd Formation and is located within a relay ramp structure (black arrow). Well-D is a side track from Well-G (not visible in Figure 3b) and deviates further away from Well-G below the top Snadd Formation horizon. Minor faults around both wells might explain differences in the observed NTG. Gamma log motifs from Well-B show good examples of stacked fining upward channels bounded by flooding surfaces.

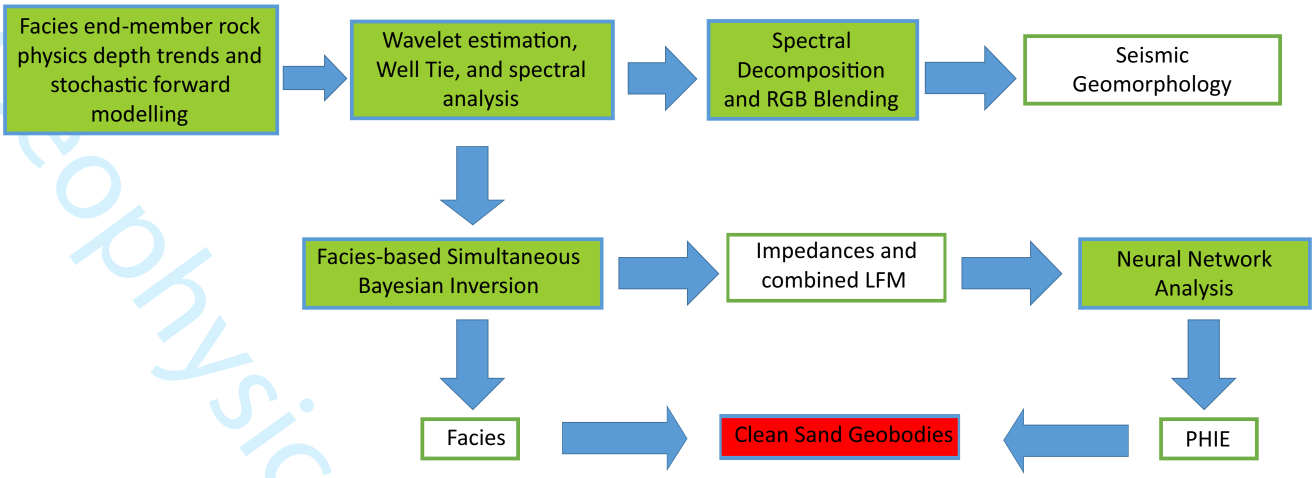

Figure 4 Workflow implemented for petrofacies and PHIE characterisation within the Snadd Formation. Depth trends play a central role in the feasibility study and during the inversion. The flow diagram shows the routes to clean sand delineation. The five main steps in the seismic reservoir characterisation workflow are highlighted in green.

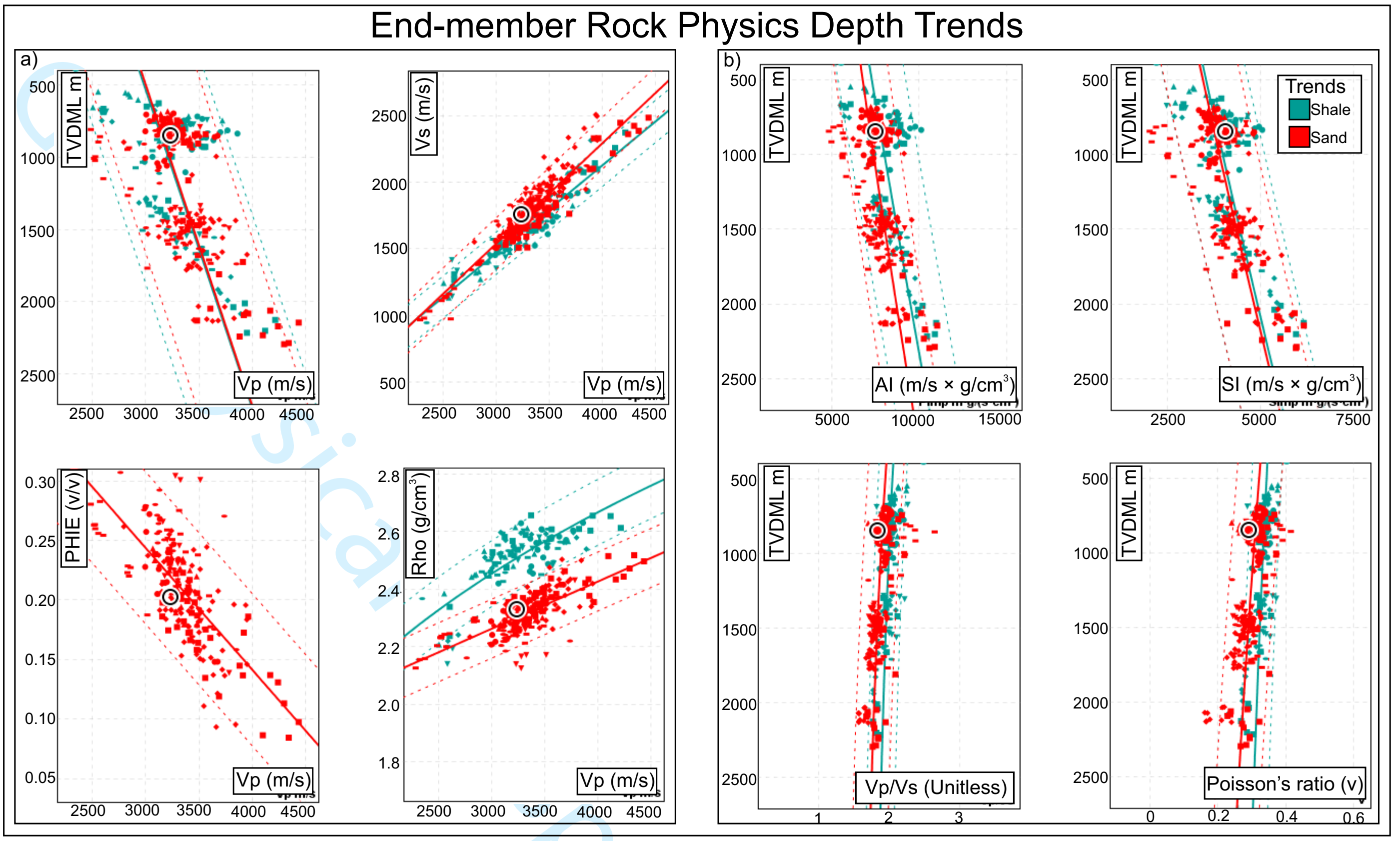

Figure 5: End-member depth trends for sand and shale through the whole well interval. The Vp, Vs, Rho, and PHIE trends are the primary trends (a) while the other trends (b) are derived from the primary trends. The sand-end member trends have been Gassmann fluid substituted to brine. The black circle shows the approximate depth location of the top Snadd Formation.

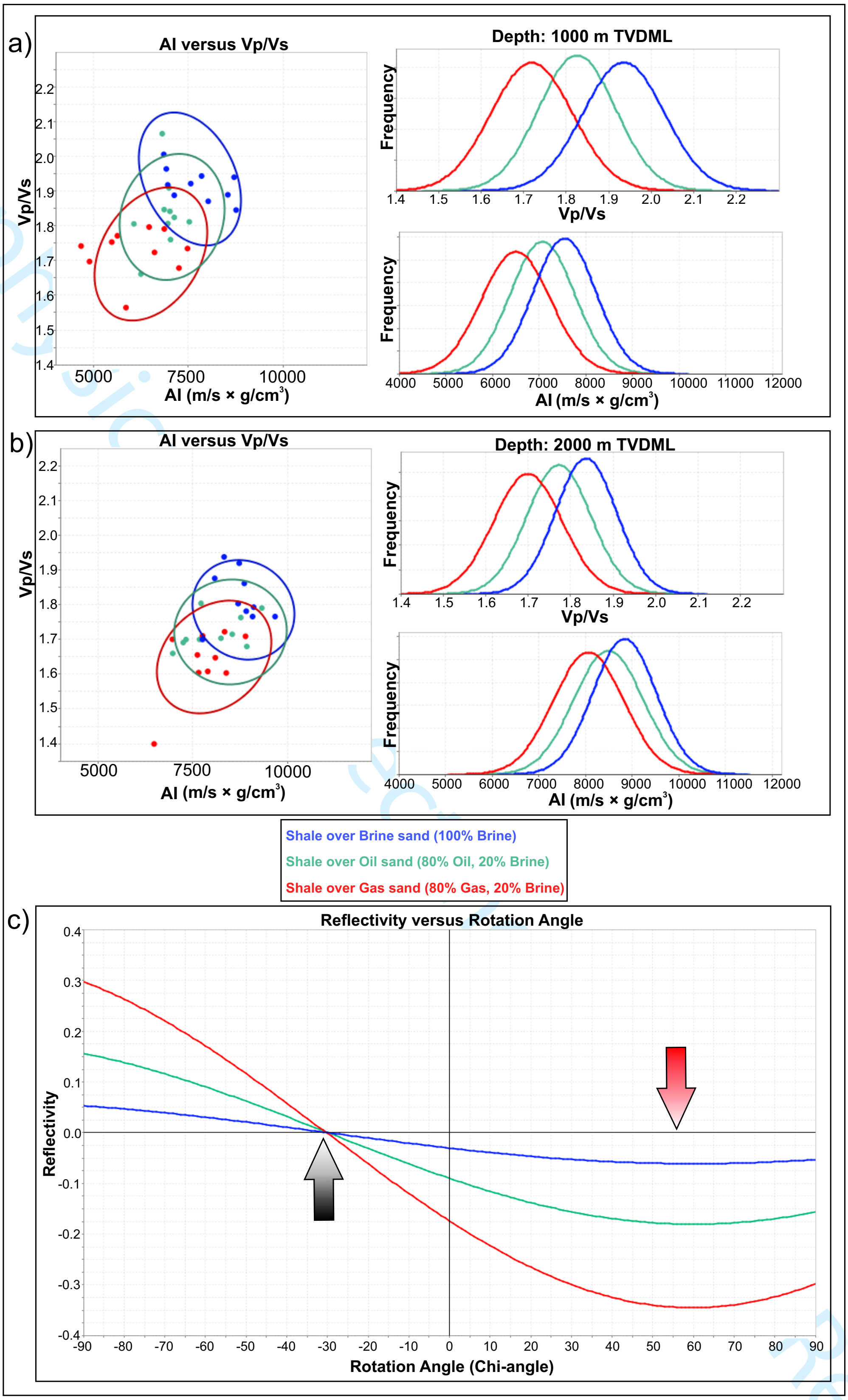

Figure 6: Depth varying PDFs (a) based on stochastic forward modelling of the end-member trends (shown in Figure 5). The plots show the fluid discrimination of AI and Vp/Vs attributes as a function of depth. Sensitivity decreases with depth as shown by increasing overlap of each ellipse and PDFs. Also the effective extended elastic impedance (EEI) chi angle (c) using the depth trends are also shown. The black and red arrows indicate the effective lithology and fluid angles.

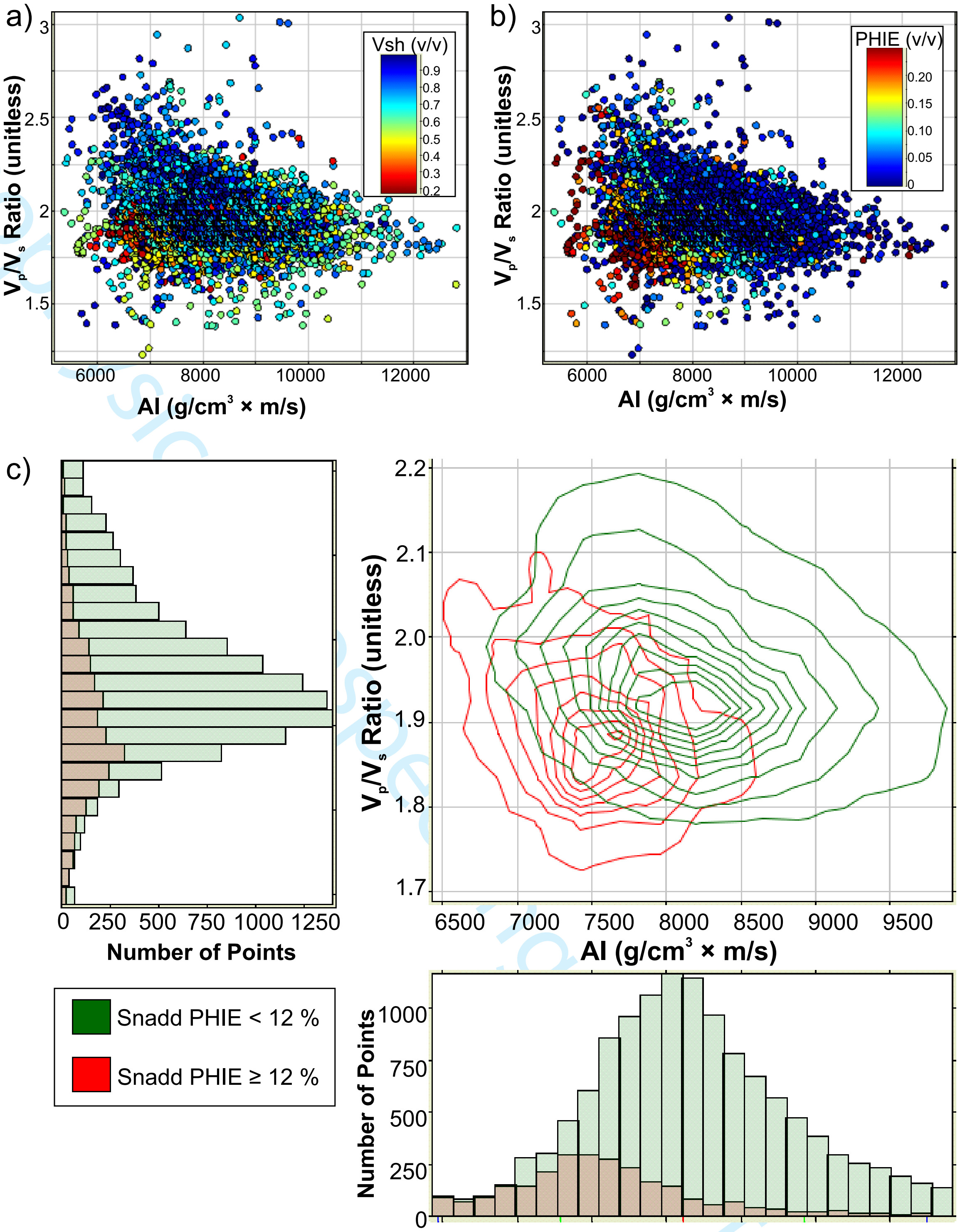

Figure 7 AI versus Vp/Vs cross plots colour coded with Vsh (a) and PHIE (b). The contour density for sand and shale are based on a PHIE cut-off using 12% as the threshold. Sands dominate at low AI and Vp/Vs ratios. However, the histograms still show a significant overlap of both facies.

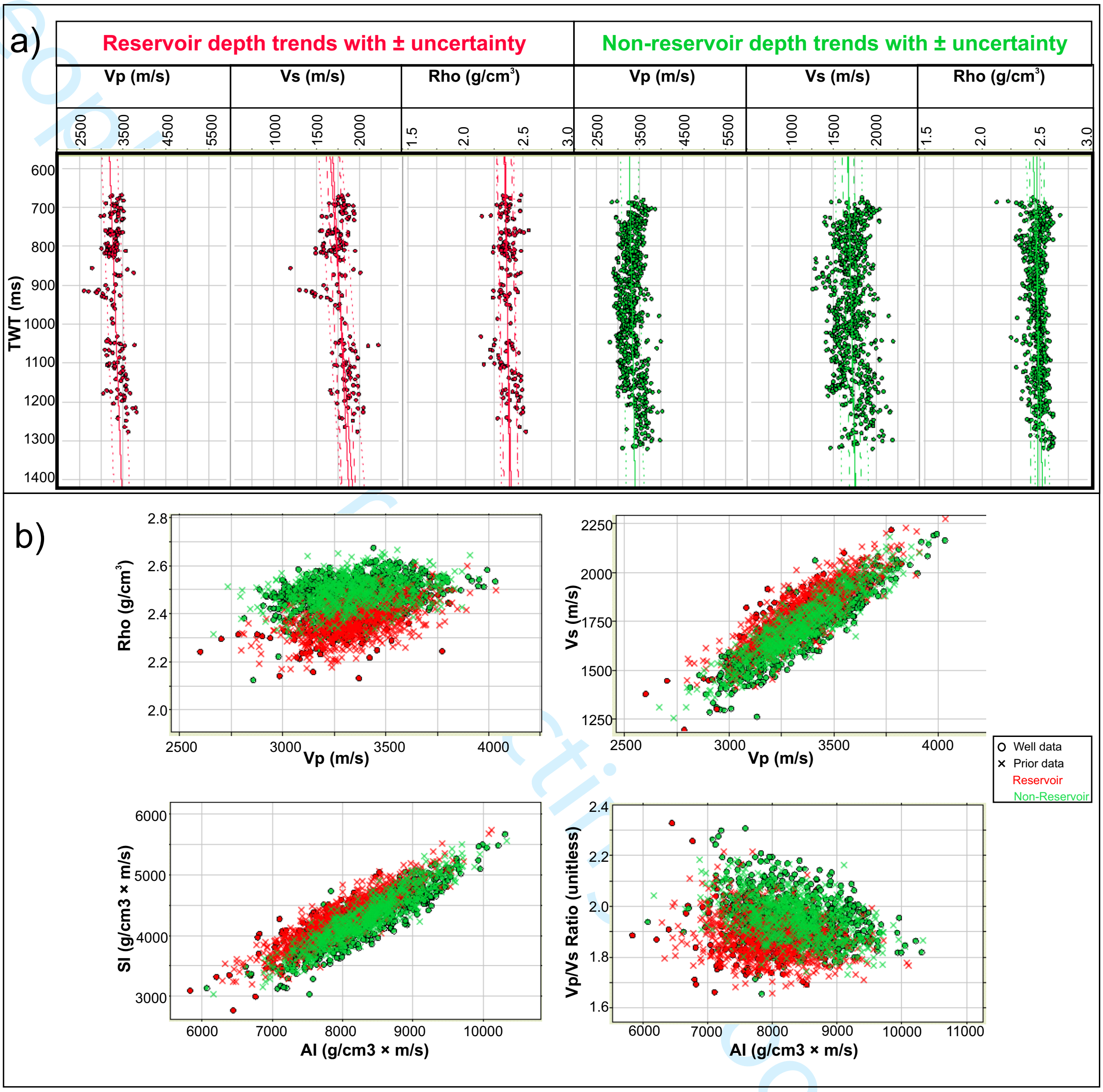

Figure 8 Reservoir and non-reservoir depth trends within the Snadd and kobbe Formation time interval. These depth trends (a) provide the uncertainty distribution of the elastic properties as a function of depth as well as the cross correlation and constraints between the elastic parameters per facies. A cross plot comparison (b) between the prior model derived from the depth trends and the corresponding well data are also shown.

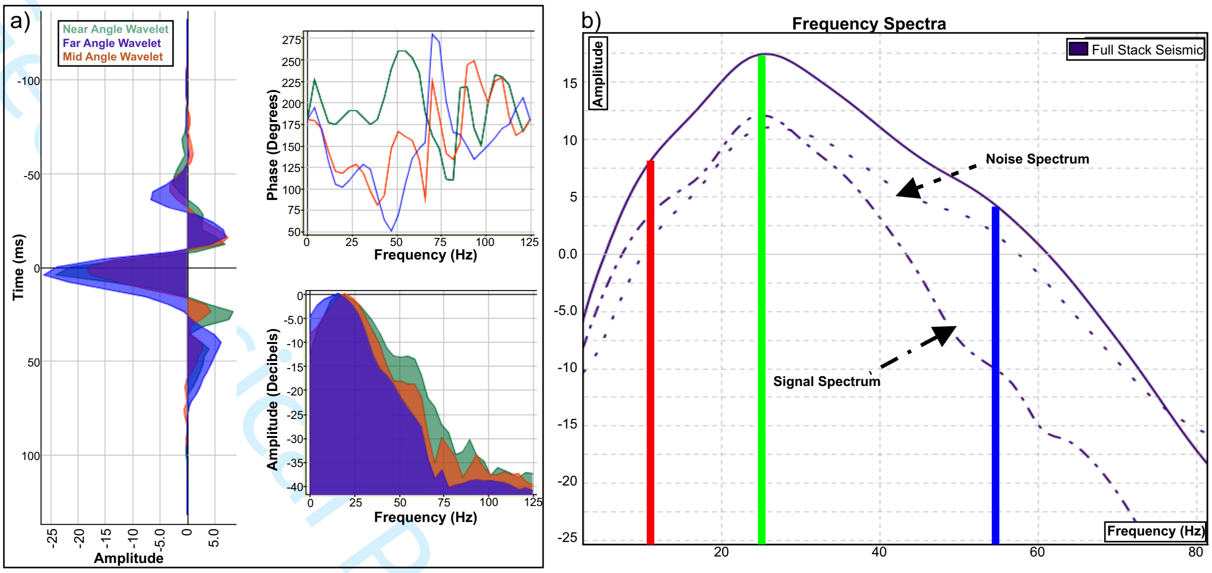

Figure 9 Wavelet processing and spectral analysis. The near, mid, and far angle stack wavelets (a) have all been extracted using the White (1980) method. The wavelets have been extracted based on the offset location with the highest PEP close to the well bore. The signal and noise spectra (b) at the top of the Snadd Formation interval are also shown with the selected frequencies used in the RGB blend.

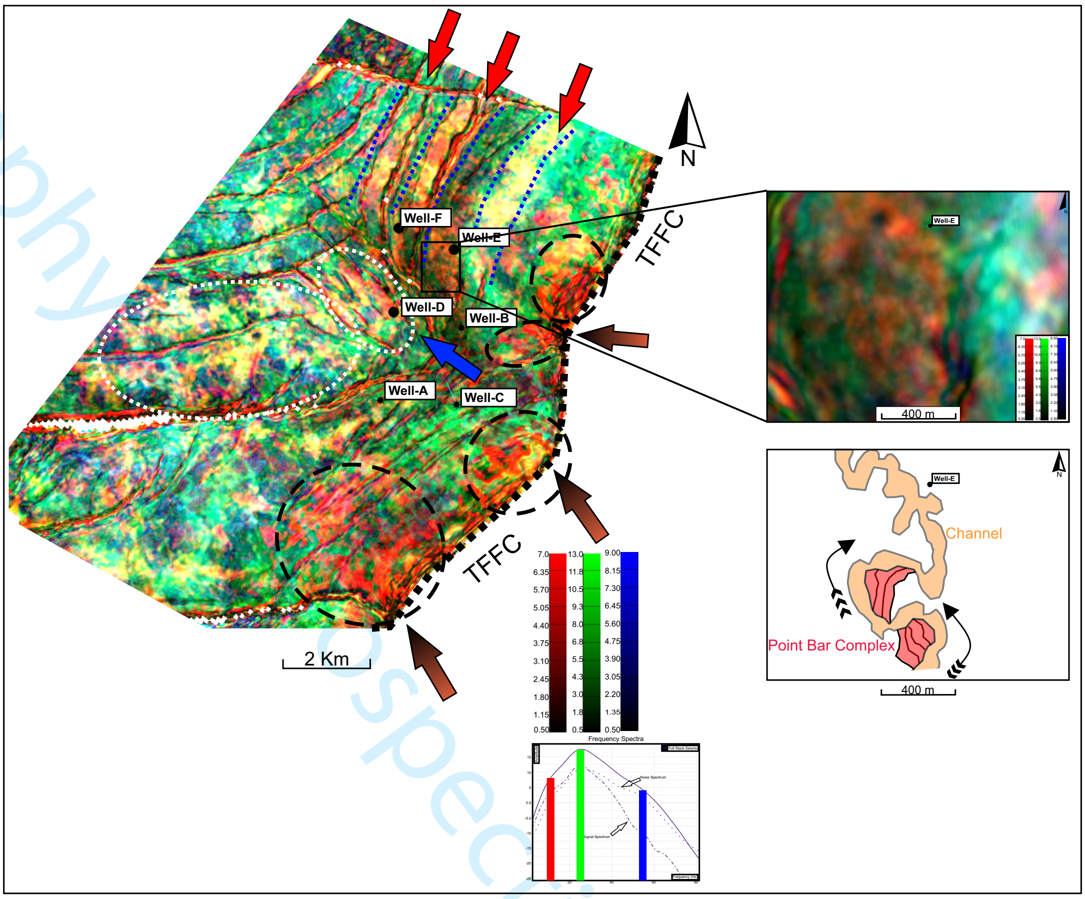

Figure 10: Spectral decomposition and RGB blending of selected frequencies displayed at the top Snadd Formation flattened horizon slice. The corresponding frequency spectra (Figure 9b) is also inserted for reference to the frequencies. The bright red arrows show a dominant NNE trend. Meanwhile close to the branching points along the Troms-Finnmark Fault Complex (TFFC), observed anomalies are oriented E-W (black dotted lines). The white dotted lines, show the anomaly around Well-D (anomalous sand proportion in Figure 3) indicated with a blue arrow. A detailed view around Well-E shows a schematic representation of a channel and point bar complex. Note that Well-E just sits at the edge of this anomaly.

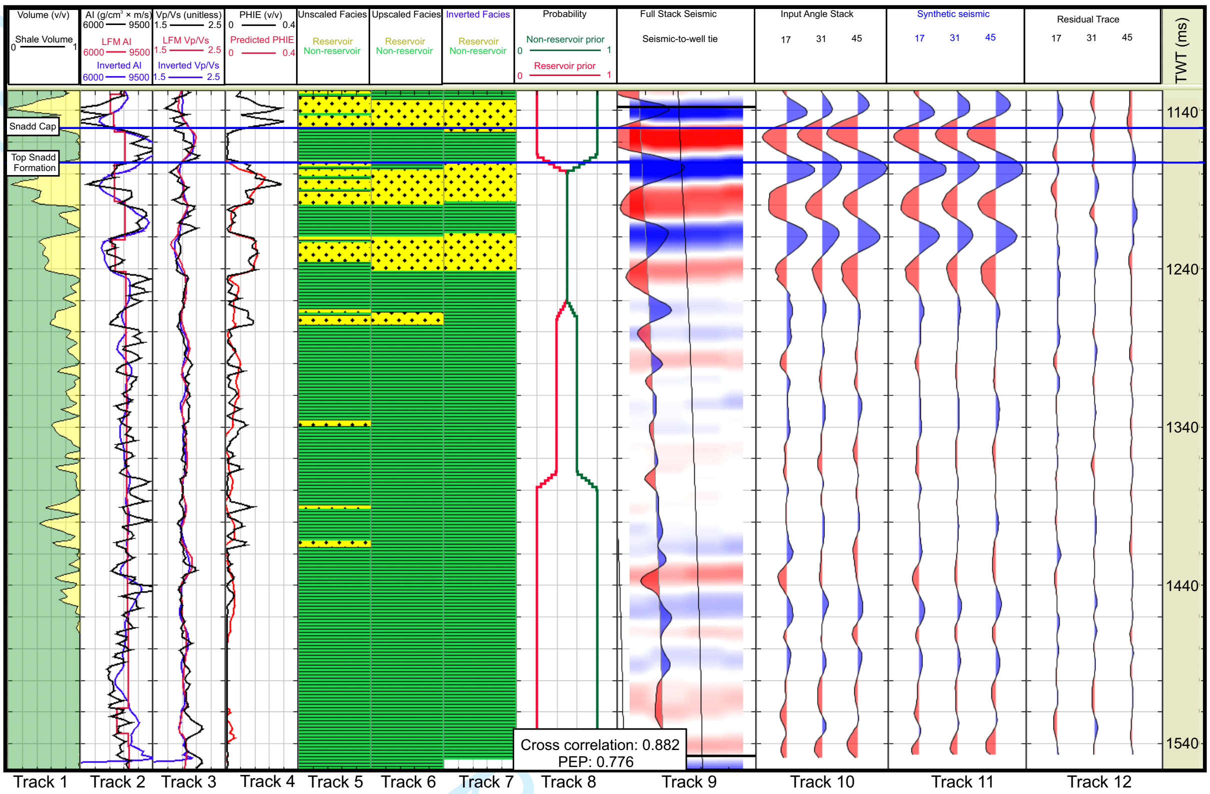

Figure 11: Facies-aware inversion and neural network results at the reference well. The inverted elastic logs (blue logs in Track 2 and 3) are plotted alongside the LFM (low frequency model) output logs (red logs) in the same tracks. There is a good match between the inverted facies log (Track 7) compared to the upscaled (Track 6). The inversion synthetic logs and the residuals are also shown in Track 11 and Track 12. The predicted PHIE log (red) from the neural network shows a match to the thicker and better developed reservoir sands (above 1240 ms TWT).

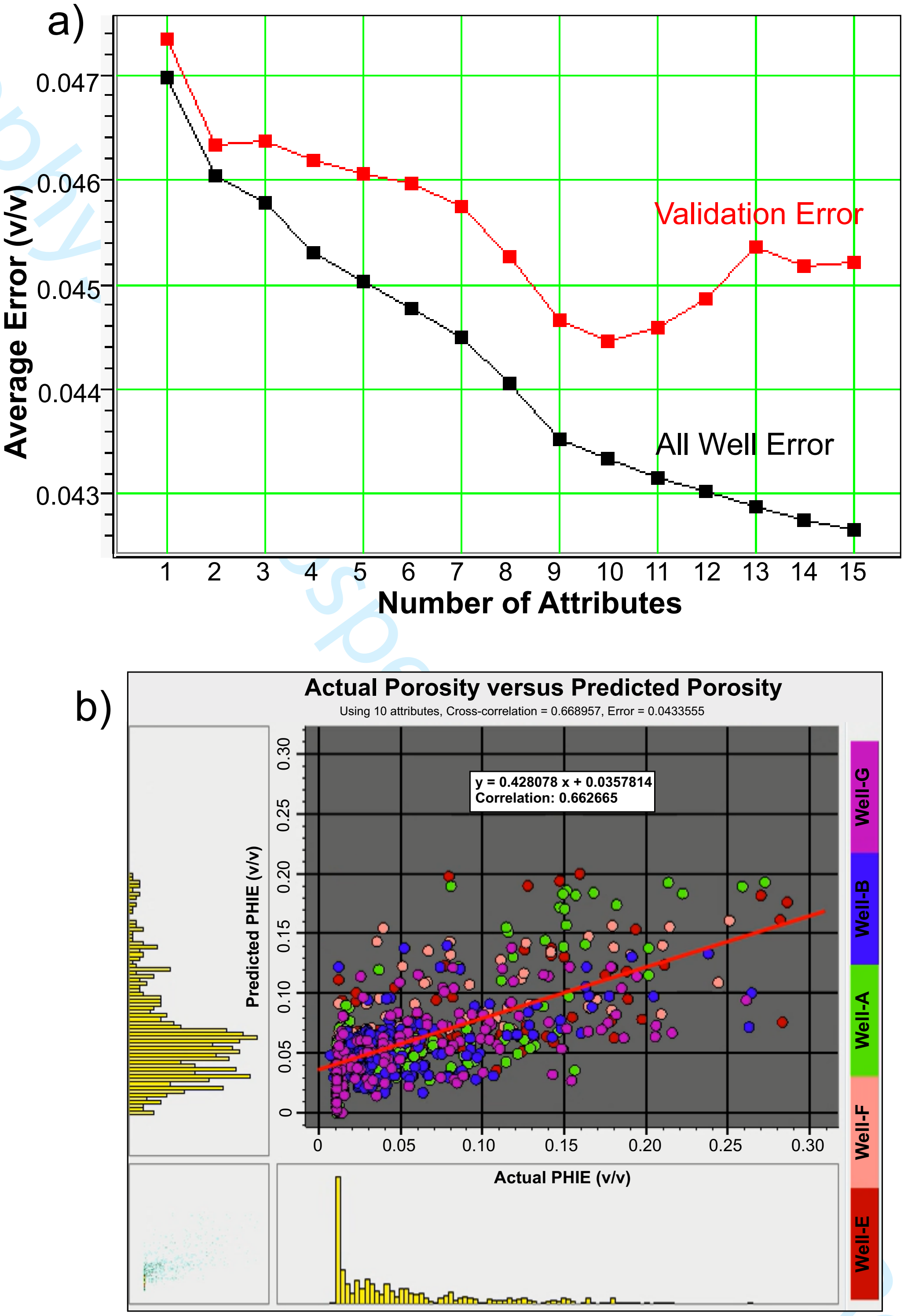

Figure 12 Multi-attribute neural network training (a) and prediction correlation (b). The validation error is shown to increase after the 10th attribute transform in the multi-attribute analysis. Attribute number 1 – 10 are used in the neural network prediction. We refer the reader to Table 2 for more details in Figure 12a.

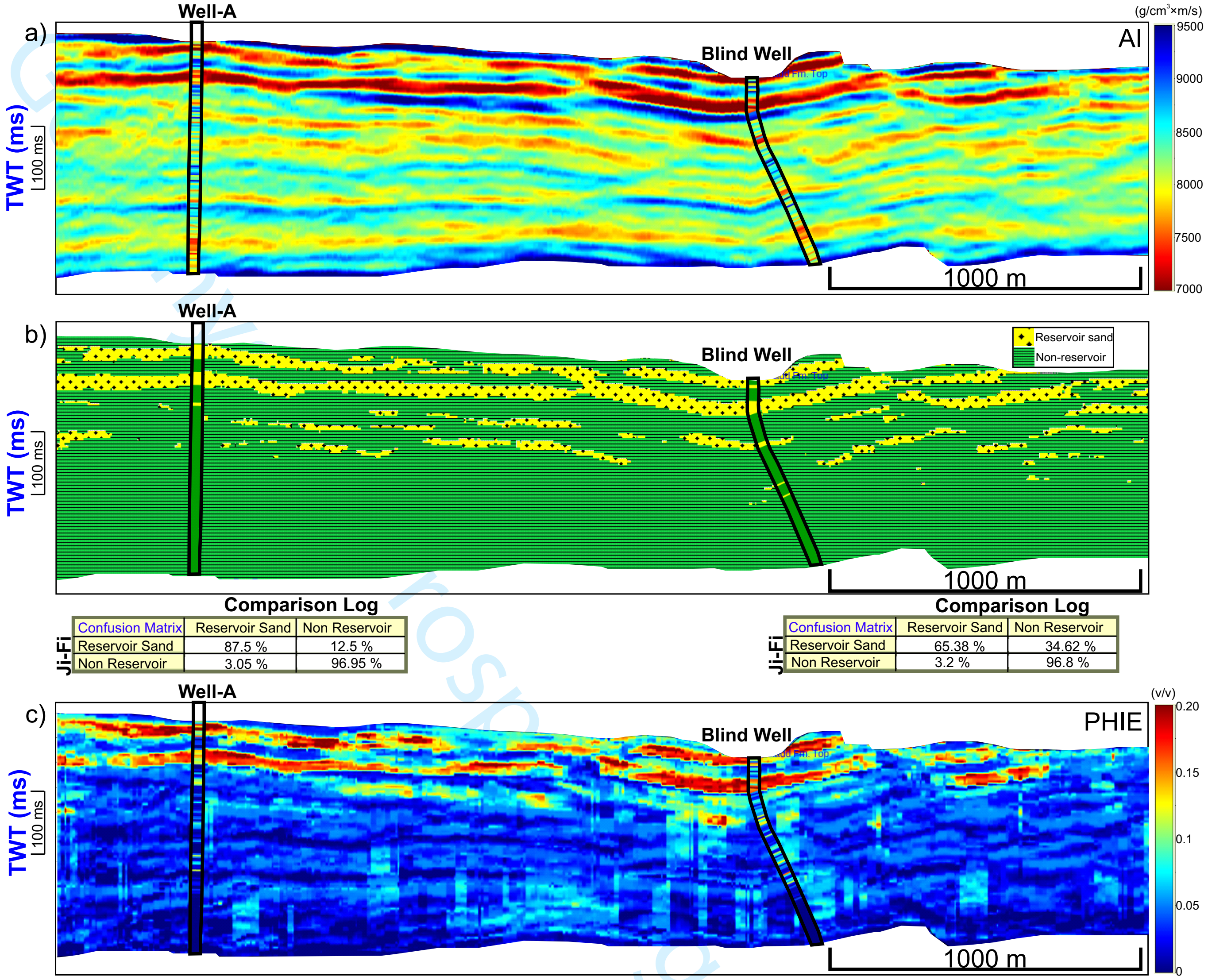

Confusion Matrix	Reservoir Sand	Non Reservoir
Reservoir Sand	87.5 %	12.5 %
Non Reservoir	3.05 %	96.95 %

Confusion Matrix	Reservoir Sand	Non Reservoir
Reservoir Sand	65.38 %	34.62 %
Non Reservoir	3.2 %	96.8 %

Figure 13 Arbitrary line section through the reference well (Well-A) and the blind well (Well-C). The simultaneous Bayesian Joint Impedance (a) and Facies (b) inversion results are compared with the neural network PHIE predictions (c). Good PHIEs observed at the upper part of the Snadd Formation (results from the neural network) are consistent with the predicted reservoir sands from the inversion. The quality of the facies predictions are illustrated in a confusions matrix below the respective wells. Diagonal elements in the matrix indicate the degree of success of the classification.

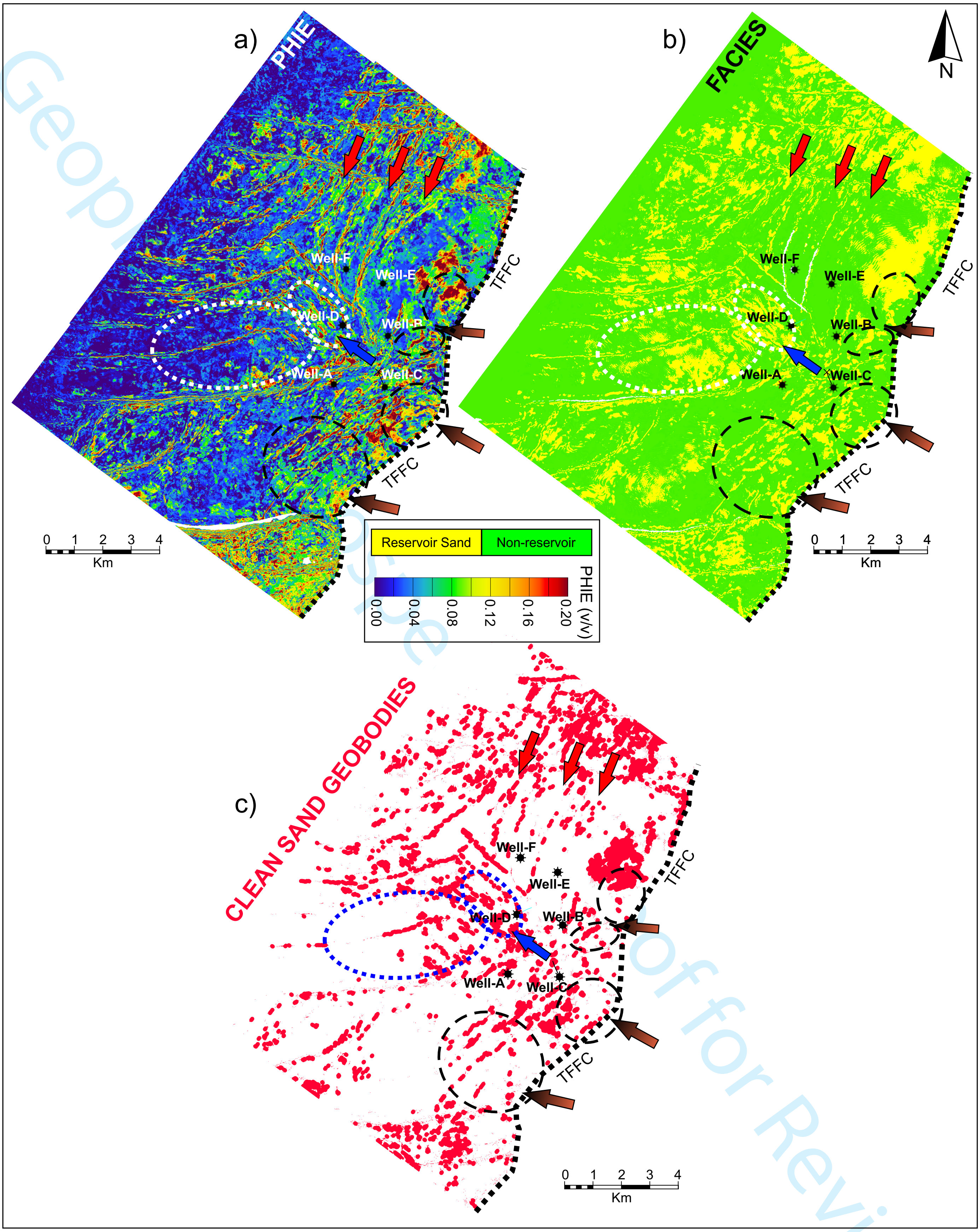

Figure 14 Horizon slices at the top of the Snadd Formation for effective porosity (a) and binary facies (b) over a 30ms window. The binary facies map is the result from the facies-based inversion, while the the porosity map is the output from the multi-layer feedforward neural network. The clean sand geobodies (c) represent predicted reservoir sand facies with PHIE greater than 15 %. Reservoir delineation is improved by qualitatively combining areas with good effective porosity in regions where reservoir sand is predicted by the inversion. The arrows and ovals from the flattened RGB slice in Figure 10, are inserted for visual comparison.

Grain/Fluid	Vp (m/s)	Rho (g/cm^3)	Vs (m/s)
Quartz	5960	2.65	3730
Brine	1500	1.05	
Oil	1100	0.8	
Gas	600	0.15	

Table 1: Grain and fluid properties used as input for brine substitution of the sand end-member trend through Gassmann's equation. Quartz properties have been used for sand end-member grain properties.

Attribute	Final Attribute Transform	Training Error	Validation Error
1	(SI LFM)^2	0.046991	0.047351
2	EEI (25°) Rotation	0.046058	0.046354
3	Derivative Instantaneous Amplitude	0.045795	0.046395
4	Filter 5/10-15/20	0.045328	0.046198
5	1/(Vp/Vs)	0.045039	0.046079
6	Dominant Frequency	0.044791	0.045984
7	Amplitude Weighted Phase	0.044515	0.045759
8	Amplitude Envelope	0.044082	0.045286
9	Second Derivative Instantaneous Amplitude	0.043540	0.044677
10	Quadrature Trace	0.043356	0.044485

Table 2: Multi-attribute transform list used as input to the neural network. Attribute numbers correspond to numbers used in Figure 13a. The attribute transform with the highest individual correlation to PHIE, is the Shear Impedance (SI) LFM output constructed during the inversion. Note that the errors associated with each successive is attribute is cumulative by applying all preceding attributes.

REPLY TO REVIEWER COMMENTS
Manuscript GP-2017-0155.R1

Special Volume "Rock-physics - From microstructure to seismic signatures"
“Integrating facies-based Bayesian inversion and supervised machine learning for petrofacies characterisation in the Snadd Formation of the Goliat Field, SW Barents Sea."

Associate Editor
“I recommend a moderate revision. Please account for the comments of reviewer #2.

Some additional comments:

- **2nd sentence of Abstract is not understandable. Please rephrase.**
  - ✓ *The sentence has been rephrased to “This is especially important when the elastic properties of the desired petrofacies significantly overlap.”*

- **Figure 12b: I suppose the predicted porosities with negative values can be excluded.**
  - ✓ *We have now disregarded the negative porosities and Figure 12b has been updated in the revised manuscript.*

- **Be consistent with acronyms. For example, PSDM is defined more than once in the text.**
  - ✓ *The second definition of PSDM has been deleted. Other acronyms in the text have also been double-checked for any repetitions.*

- **In many places the manuscript reads like a technical report. You often use "generally helps", "is usually done" or the like. This makes it hard for the reader to understand what your original contribution is, when you follow a standard workflow or when you use results of others. I would like to encourage you to use more active language.**
  - ✓ *Selected sections of the text have been rephrased with more active tenses. These changes can be seen in the annotated revised manuscript.*

Reviewer: 1

- **“I think the content of this paper qualifies for the publication. Please double check the citations in the text to match those in the references**”.
  - ✓ *The in-text citations have been checked for consistency and five references were updated. These changes are highlighted in the revised manuscript.*

Reviewer: 2

Major comments

- **“If the main objective of a study is a combination of different sources of information to map out reservoir sands then I would expect such a final map to be presented by**

the authors or alternatively some information about how disagreements between the different sources of information would be handled to obtain such a final map”.

- ➢ *A final map has now been included (Figure 14c) showing clean sand geobodies extracted based on the inversion-derived binary facies, and PHIEs from the neural network i.e reservoir sand prediction AND PHIEs >15% represent “clean sand geobodies in Figure 14c.*

- **“A workflow for me implies that the results obtained in step 4 are used in step5. It needs to be clarified that this is not the case as stated by the authors in the reply to reviewers' comments”**.
  - ➢ ***Step 5*** *“Supervised neural network for porosity estimation” uses the elastic parameters derived from* ***Step 4*** *“Facies-based Bayesian inversion to predict absolute elastic properties and facies”. This is also evident in the Final Attribute Transform list in* ***Table 2****. For example,* ***Attributes 1 and 5*** *are transforms of outputs derived from the facies-based inversion in* ***Step 4.***

  - ➢ *With respect to the previous reply to reviewers’ comments, We would like to clarify that the neural network has NOT been used to improve the elastic property prediction obtained from the facies-based inversion. Rather, the elastic properties from the inversion have been used as an input for the PHIE prediction in the neural network. We hope this explanation clarifies the workflow shown in Figure 4.*

- **“It is alson not clear why the fullworkflow consists of less steps than the summary workflow (Figure 4) and does not show the branching of the summary workflow”.**
  - ➢ *The words “****summary and full****” have been removed from the caption in* ***Figure 4*** *and in the text. The 5 main processes listed in the text have now been given a different colour. In addition, the branching has been modified to hopefully provide better clarity. We hope this further clarifies the workflow figure*

- **“Figure 2: The caption refers to a vertical change in net-to-gross. Is this the well log superimposed on the Full Stack Seismic? If so, this needs to be clarified in the figure”.**

  - ➢ *This part of the figure caption has now been rephrased to. “The vertical change in the net-to-gross (as seen from the Sand Flag log track) effectively divides the interval into three main lithological zones (b).*

  - ➢ *The well log track shown on the full stack seismic is the P-impedance log. This is now specified as well in the Figure caption “The P-impedance log is superimposed on the full stack seismic section”.*

Minor comments

- **Page 1 "within the limmits of the seismic bandwidth. Meanwhile the effective" limmits-> limits**

- **Page 14 "These frequencies where selected based on the dominant" where -> were**

  - ✓ *These have now been corrected to “****limits****” and “****were*** *“respectively.*

Integrating facies-based Bayesian inversion and supervised machine learning for petrofacies characterisation in the Snadd Formation of the Goliat Field, SW Barents Sea.

Honoré Yenwongfai [2,1], Nazmul Haque Mondol [1,3], Isabelle Lecomte [4], Jan Inge Faleide [1], Johan Leutscher [5]

[1] *University of Oslo,* [2] Statoil ASA, [3] Norwegian Geotechnical Institute, [4] University of Bergen, [5]Eni Norge.
Contact email: hyen@statoil.com

ABSTRACT

Seismic petrofacies characterisation in low net-to-gross reservoirs with poor reservoir properties such as the Snadd Formation in the Goliat field, requires a multidisciplinary approach. This is especially important when the elastic properties of the desired petrofacies significantly overlap~~desired petrofacies of interest overlap significantly in a rock physics elastic space~~. Pore fluid corrected end-member sand and shale depth trends have been used to generate stochastic forward models for different lithology and fluid combinations in order to assess the degree of separation of different petrofacies. Subsequently, a spectral decomposition and blending of selected frequency volumes reveal some seismic fluvial geomorphological features. We then jointly inverted for impedance and facies within a Bayesian framework using facies-dependent rock physics depth trends as input. The results from the inversion are then integrated into a supervised machine learning neural network for effective porosity discrimination. Probability density functions derived from stochastic forward modelling of end-member depth trends show a decreasing seismic fluid discrimination with depth. Spectral decomposition and blending of selected frequencies reveal a dominant NNE trend compared to the regional SE – NW progradational trend, and a local E-W trend potentially related to fault activity at branches of the Troms-Finnmark Fault Complex. The facies-based inversion captures the main reservoir facies within the ~~limmits~~limits of the seismic bandwidth. Meanwhile the effective porosity predictions from the multilayer feedforward neural network are consistent with the inverted facies model, and can be used to qualitatively highlight the cleanest regions within the inverted facies model. A combination of facies-based inversion and neural network improves the seismic reservoir delineation of the Snadd Formation in the Goliat Field.

Keywords: Inversion, rock physics, facies, reservoir characterisation, neural network

INTRODUCTION

The Norwegian Barents Shelf (NBS) is a frontier hydrocarbon exploration province when compared to the other parts of the Norwegian Continental Shelf (NCS) such as North Sea and Norwegian Sea. The NBS has a far more complex burial history, with differential amounts of uplift and erosion within the different basins, platform areas and local highs. Uplift and erosion introduce additional challenges and uncertainties when evaluating the petroleum system with respect to cap rock integrity, source rock maturation, and overconsolidation of the target reservoirs with respect to the present day depths. Understanding and constraining rock physics depth trends is crucial in areas with such a complex burial history.

The Goliat Field is located about 85 km southeast of the Snøhvit gas field (Figure 1) in the Norwegian sector of the Barents Sea. It is the first oil field in the Norwegian sector of the Barents Sea to be in production (March 2016). The majority of the NBS discoveries indicate a dominance of gas over oil. The oil reserves in the Snadd Formation of the Goliat field were not included in the Plan for Development and Operations (PDO). As a result, the Snadd Formation has not been the focus in earlier studies from a quantitative seismic petrofacies characterisation perspective. However, a better understanding and delineation of the fluvial sand facies at the top of the Snadd Formation should provide additional insight into the porosity distribution for the cleanest sand intervals.

From a geophysical perspective, the Snadd Formation is challenging for the seismic lithology and fluid characterisation for three main reasons; i) relatively thin, silty-shaly sandstone units not ideal for AVA (Amplitude Versus Angle) analysis, ii) significant petrofacies overlap in rock physics elastic properties, and iii) overconsolidated reservoir due to uplift stiffens both the rock frame and pore space, thereby reducing the seismic fluid sensitivity. The main objective of this study is to discriminate and map out clean reservoir sands within the Snadd Formation using a multidisciplinary workflow combining spectral analysis, facies-based Bayesian inversion and supervised neural networks.

GEOLOGICAL SETTING

The Uralian mountain chain is one of the last collision elements close to the study area in Permian-Triassic times and represents an important source area for the dominantly siliciclastic sediments. Collapse and erosion of this orogeny, together with sediments from the basement rocks in the Kola peninsula, gradually filled the Barents Sea area mainly from the southeast (Mørk 1999; Glørstad-Clark et al., 2010; Henriksen et al., 2011b).

Structurally, the Troms-Finnmark Fault Complex (TFFC) is one of several regional faults in the area (Figure 1) and it cuts across the Goliat Field. The TFFC has a series of listric normal faults (Faleide et al., 1984; Gabrielsen, 1984; Gabrielsen et al., 1990; Mulrooney et al., 2017) forming a prominent roll-over anticline which provides structural closure for the field. Later Cenozoic uplift and exhumation in the Goliat area resulted in approximately 1000 to 1500 m of net erosion (Ohm et al.,2008; Henriksen et al., 2011b; Baig et al., 2016). This implies that the reservoirs have been exposed to much higher pressures and temperatures (i.e., more mechanical and chemical compaction) than at their present depths.

As mentioned earlier, the Snadd Formation is the main focus in this study (Figure 2a). The Barents Sea was part of a large and shallow inland sea, during the time when the Snadd Formation was deposited in the Late Ladinian to Early Norian (Dalland et al., 1988). According to Glørstad-Clark et al. (2010), the main depocenter during this time was located around present day Loppa High.

The regional sequence stratigraphic framework for the Snadd Formations has been documented by several authors (Glørstad-Clark et al., 2010; Klausen et al., 2015). The chronostratigraphic subdivision of the Snadd Formation is based on regionally correlated maximum flooding surfaces (MFS). The Top Snadd Formation sands in the Goliat field are capped by shales of the Fruholmen Formation. It represents the boundary between the Late Triassic Carnian and Norian Stages. This capping shale unit shows a characteristic higher acoustic impedance (AI) than the underlying Snadd Formation sands (Figure 2b). This results to a strong negative reflection coefficient. Note that positive amplitudes represent negative reflection coefficients in Figure 2b due to the reverse polarity of the data. The upper part of the Snadd Formation ~~generally~~ contains thicker and cleaner sands, as opposed to the middle section with more heterolithic or thin interbedded ("ratty") sands and shales. The base of the Snadd Formation (Ladinian) overlying the Kobbe Formation is dominated by marine shales. This gross vertical change in the sand proportion can easily be seen by looking at the gamma ray log and sand flag (Figure 2b). The Snadd Formation has a southeast to northwest regional depositional dip (Riis et al., 2008; Glørstad-Clark et al., 2010; Klausen et al., 2015). The boundary between the Snadd Formation and the Kobbe Formation (Anisian to Early Ladinian) below, is characterized by a drop in AI from the basal anoxic shales of the Snadd Formation to the sand prone Kobbe Formation.

The systematic change in the depositional environments for the Snadd Formation, from open marine at the base to non-marine fluvial sediments at the top, translates into an ~~general~~ increase in the net-to-gross (NTG) and quality of the reservoir sands towards the top of the formation. A north – south correlation profile through the available wells is shown in Figure 3a. The wells tops are flattened at the top Snadd Formation pick. Small-scale internal flooding surfaces can be seen bounding a series of stacked fining upward channel sands (blue arrows in the zoomed view in Figure 3a) based on the gamma ray log motif. The NTG at one of the deviated wells (Well-D) shows an anomalous proportion of sand within the Snadd Formation. The same outlier well is located structurally lower in a down – faulted segment compared to the other wells and is bounded by a relay-ramp fault system (Figure 3b).

DATABASE AND METHOD

Long-offset multi-azimuth (MAZ) 3D seismic, wireline logs, prestack depth-migrated (PSDM) velocities, and stratigraphic horizons were provided by the PL229 licence. The MAZ (127°, 67°, and 7°N) 3D seismic data over the Goliat Field each covers an area of approximately 209 km^2. During the processing of the seismic data (Buia et al., 2010), the partial angle stacks from the individual azimuths were rotated and referenced to 127°N (consistent with previous older survey azimuth). The near-angle (17°), mid-angle (32°), and far-angle (45°) partial stacks from each rotated azimuth are stacked to provide high quality angle stacks used as input in this study.

The well database consists of seven exploration and appraisal wells. Of these seven wells, two are not drilled through the entire Snadd Formation. Two of the remaining wells (oil- and brine-filled within the Snadd Formation) have been drilled through the entire formation, and in addition contain measured V_s logs. The relevant elastic logs of compressional velocity (V_p), shear velocity (V_s) and bulk density (Rho), alongside a suite of other formation evaluation logs (gamma ray, resistivity, porosity, etc.) have been used for petrofacies characterisation and discrimination during the feasibility analysis. A summary of the data-driven multidisciplinary method used to delineate clean sand units in the Snadd Formation is shown in Figure 4. The ~~full~~ workflow can be subdivided into the following main steps:

1. End member depth trend analysis and stochastic forward modelling,
2. Rock physics feasibility and facies discrimination
3. Well –to – seismic ties and spectral decomposition for seismic geomorphology
4. Facies-based Bayesian inversion to predict absolute elastic properties and facies.
5. Supervised neural network for porosity estimation

End-member depth trends and stochastic forward modelling

A rock physics feasibility analysis ~~generally helps~~is important in identifying the appropriate quantitative interpretation strategy for the different gross depositional environments within a given basin. This ~~is usually~~can be done ~~through~~ using crossplots between various well log elastic properties and geological variables like porosity, volume of shale, and water saturation. The degree of facies separation in different elastic domains as a function of depth, provides clues as to which elastic parameters best discriminate the facies of interest. Siliciclastic sediments dominate the

Triassic Snadd Formation. As a result, end member sand and shale facies (Figure 5) have been picked in all the available wells spanning drilled depth. These end-member picks represent the cleanest example of a specific lithofacies. These picks are based on drilling reports, and the full suite of measured and computed petrophysical logs. For the clean sand end-member, the variation in pore fluid properties are also taken into account. The Backus average for each picked zone in the well is used as a single point in the end-member depth trend. During the manual picking process, the relative quality of each end-member pick is assessed from how close the individual pick histogram is to a normal distribution. This ensures that small unusual outliers are not considered and leads to more robust and representative end-member trends.

Once the representative depth trends are obtained for the in situ fluids, Gassmann (1951) fluid substitution is then applied (i.e., referencing all the fluid trends to brine) to effectively remove the scatter in the elastic property depth trends due to variations in the fluid type. The quartz grain and pore fluid properties used for fluid substituting the sand end-member trends are shown in Table 1. The effective porosity and saturation for each zone pick is obtained from the well logs. The dry rock bulk modulus is inverted for (using Gassmann's equation), given the moduli of quartz and porosity. As a result of a varying porosity input, the inverted dry rock bulk modulus also varies as a function of depth. The final brine-filled, end-member depth-dependent trends can then be used as input to construct i) depth varying stochastic Amplitude Versus Angle (AVA) forward models, ii) depth dependent Gaussian Probability Density Functions (PDFs) of the absolute elastic properties, and iii) the effective Extended Elastic Impedance (EEI) rotation angles (Whitcombe et al., 2002) for lithology and fluid stacks at different depths of investigation.

Formatted: Highlight

The stochastic forward models (Figure 6) are based on random sampling from the PDFs at the target depth, between a specified lithology and fluid composite (litho-fluid) across an interface.

This stochastic forward modelling analysis goes beyond the end-member brine trends, but can also include desired or expected litho-fluid composites at different depths. These trends are important in understanding the key elastic parameters controlling the facies discrimination as a function of depth. The depth varying PDFs can later be used to classify the inverted volumes, or other prestack data cross plot combinations (i.e., AVA intercept and gradient, near- versus far-angle stacks), to the desired facies of interest.

These end-member depth trends may be utilised directly in building the very important low-frequency model (LFM) required to obtain absolute elastic properties from a model-based inversion. This requires good prior knowledge of the NTG, which is then used to specify the representative proportions of the end-member trends within each stratigraphic interval. The challenge in doing so is that the NTG distribution within the Snadd Formation is the main objective of the study and the reason for inverting in the first place. As a result, we adopt a different approach to obtain the required low-frequency model, which is explained in the facies-based simultaneous inversion section of the workflow. Prior to the facies-aware inversion, we need to define the target petrofacies from available well data and assign depth dependent rock physics trends.

Petrofacies classification and per-facies depth trend analysis

Rock physics crossplots such as AI versus V_p/V_s ratio, colour coded with shale volume and porosity (Figure 7a and Figure 7b respectively), have the potential to reveal facies clusters or trends in petroelastic space. Deciding on the number of petrofacies to invert for is not always trivial. There is a trade-off between the number of different petrofacies needed for subsurface characterisation and the resolution limitations (i.e., narrow bandwidth compared to well log data) of the seismic.

A binary petrofacies log has been created using effective porosity (PHIE) cut-off (PHIE < 12% represent non-reservoir) to distinguish reservoir from non-reservoir. This cut-off is based on how well the derived facies classes separate in the elastic domain. The corresponding AI versus V_p/V_s PDFs of the binary facies are shown in Figure 7b. This binary log was subsequently upscaled based on filtering the PHIE log using a Gaussian function over a 15-m window, and subsequently applying the same cut-off. The upscaled log is used at a later stage for comparison to the inversion-derived facies log at the well locations. Meanwhile, the unscaled facies log is used to define per facies rock physics depth trends. Figure 8a shows the depth trends (using only five vertical wells) for reservoir sand and non-reservoir facies within the Snadd and Kobbe formations interval. Two deviated wells were left out of the depth trend analysis. One of these wells is used as a quality control (QC) blind well for the inversion and neural network predictions. The depth trend analysis provides, i) the prior facies proportions for subsequent facies-based Bayesian inversion, ii) uncertainty distribution (dotted line in Figure 8a) in the elastic properties per facies with depth, and iii), per-facies rock physics cross correlations (Figure 8b) between V_p, V_s, and Rho. The prior probabilities obtained from the depth trends are used as initial estimates only and ~~they usually need to be~~are adjusted down slightly to account for bias in well placement (since available wells target areas with expected high NTG). The uncertainty distribution of the elastic properties with depth and the corresponding cross correlations provide important facies-dependent constraints during the Bayesian facies-aware simultaneous inversion process.

Well-to-seismic ties and spectral analysis

Well ties represent a crucial step in understanding the relationship between the seismic amplitudes and the impedance contrasts at the wells. This requires a comparison between a synthetic seismic trace and the seismic trace at the well location. The convolutional forward model needed to create the synthetic trace requires a wavelet. This wavelet can either be derived statistically without using the wells (assuming the seismic data is zero phase), or using a deterministic approach using wells (no assumption of the phase of the data). For this work, we have used the White (1980) method to estimate the wavelets shown in Figure 9a. This deterministic method provides the appropriate wavelet scaler required to link the reflection coefficients computed at the wells to the corresponding observed seismic amplitude. The elastic logs (V_p, V_s, and Rho) are Backus averaged to the seismic bandwidth prior to convolving with the derived wavelet. The quality of the tie is quantitatively assessed using attributes such as the Proportion of Energy Predicted (PEP) and the cross correlation coefficient. The Root Mean Square (RMS) error of the wavelet obtained for each angle stack is used during the inversion to weight the contribution of the near-, mid-, and far-angle stacks differently. The signal-to-noise (SNR) at the target is estimated from the PEP following,

$$SNR = \sqrt{\frac{PEP}{1-PEP}} \qquad (1)$$

A spectral decomposition is then carried out on the full stack data. This decomposes the seismic traces to user defined constituent frequencies through a Fourier transform operation within the target window for the Snadd Formation. Analysis of the resulting amplitude spectrum (Figure 9b) and the frequency cube over sand rich intervals around the wells provide insight into which frequencies to select for a Red – Green – Blue (RGB) frequency blend. Seismic geomorphologic features of interest are subsequently highlighted based on an RGB flattened horizon slice for the top Snadd Formation.

Facies-based simultaneous Bayesian inversion

Seismic data is well known to be bandlimited. However, the low-frequency component of the seismic data is more crucial to the successful application of absolute seismic inversion schemes (Cooke and Schneider, 1983). These low frequencies contain the subtle compaction trends, which, if not properly captured, will result in erroneous estimates of the absolute elastic properties, irrespective of the optimisation inversion algorithm used.

Several practitioners over the years have used different methods to obtain this crucial low-frequency component of the earth. One method is to apply a high-cut frequency to horizon guided interpolations of well log elastic properties. The quality of the LFM is dependent on the number and spacing of the wells. Other methods use seismic velocities (stacking or ~~Prestack Depth Migrated (~~PSDM~~)~~ velocities), either as a standalone input, or co-krigged with the well logs (Yenwongfai et al., 2017a). The seismic Rho and Vs LFMs can be subsequently obtained by applying rock physics transforms such as the Gardner et al. (1974) and Castagna et al. (~~1988~~1998) equations, respectively. The pitfall in using seismic velocities alone is that the corresponding LFMs for Vs and Rho do not contain any independent information. Therefore, in geologic scenarios where the primary facies discriminating parameter is V_p/V_s ratio, the inversion for the purpose of facies discrimination is compromised before one begins. Another method could be to use facies dependent end-member trends as input. The challenge here, as mentioned earlier, is in specifying the correct proportion of the end members, for each zone of interest, to obtain one average LFM. However, it is beyond the scope of this paper to discuss the pitfalls in constructing the LFM or a review of different inversion methods. We refer the reader to Sams and Carter (2017) for more details and alternative methods for constructing a LFM. In addition to the challenges in constructing a LFM, classical inversion algorithms treat the problem as only continuous (impedances), and ignoring facies (discrete) which together drive the seismic response.

In order to overcome these limitations, Kemper and Gunning (2014) introduced a novel approach where the impedances and facies are jointly inverted for in a Bayesian framework. The same method was applied in this study. Here, the LFM is an output (constructed during the inversion) and not an input. Facies-dependent depth trends for V_p, V_s, and Rho are used to construct two LFM representatives for reservoir sand and non-reservoir facies in the Snadd Formation. This ensures that the compaction trends and the associated uncertainty with depth is accounted for per facies. For a detailed review on the inversion scheme, we refer the reader to Kemper and Gunning (2014).

Once facies are obtained, inverse rock physics models per facies (Johansen et al., 2013) can be applied to the inverted facies result to obtain petrophysical parameters like shale volume (Vsh), PHIE, and water saturation. For good results, core data calibration is often required. In the absence of available core data, multi-attribute analysis and neural networks were used to combine all available data into one analysis and search for non-linear trends in the data.

Supervised neural network

Neural networks have the advantage of exploiting complex non-linear relationships between multiple input parameters to predict a target output. Step-wise linear regression based algorithms might miss some important non-linear information vital for reservoir properties such as PHIE. Utilising neural networks or multi-attribute seismic analysis for lithology characterisation is not new (e.g., Hampson et al., 2001; Pramanik et al., 2004). However, there has been an increasing trend in integrating seismic inversion products with machine learning algorithms to squeeze out more subsurface information.

The main objective of the supervised neural network in this study is to put together in one analysis all relevant attributes derived from the inversion which are indirectly related to the pore volume.

A three-layer feedforward network has been used with a total of 15 nodes in the hidden layer. A sigmoid activation function has been used. The training process is done in time and requires a seismic consistent sampling rate (4 ms in our case) for the target porosity logs (computed from logs measured in depth). Good seismic–to–well ties are crucial during the training phase. First, single attributes are compared and ranked based on their correlation with the PHIE log at the training wells. Then, several multi-attribute combinations are compared and ranked according to the training and validation errors. The optimum number of attributes are chosen based on the validation error profile associated with the successive addition of attributes to the training process. This step tries to reduce the risk of over classifying the attributes in the final neural network. This optimum attribute set is then used as input to the multi-layer feed-forward neural network (MLFN). Optimisation of the cost function is achieved through a combination of conjugate gradient and simultaneous annealing algorithms to search for the global minimum. Meanwhile the optimum synaptic weights between the nodes are derived during the training, by backpropagation of the error in the predicted log when compared to the actual porosity log. The final extracted clean sand geobodies are based on PHIEs > 15 % within the reservoir sand predictions obtained from the facies-based inversion.

RESULTS AND DISCUSSION

Figure 5 shows Gassmann corrected end-member depth trends for sand and shale. All the trends are referenced to brine and plotted from the mudline. The dotted lines represent two standard deviations from the mean trend (solid lines). The black circle on the depth trends represent the approximate top Snadd Formation. As expected, both V_p trends for sand and shale increase as a function of depth due to increasing mechanical (stress dependent) and chemical (temperature and time dependent) compaction with burial. The porosity loss with increasing burial depth is also captured in the inverse relationship between V_p and PHIE. The end-member trends for P-impedance and Poisson's ratio (ν) become more unique at burial depths greater than that represented by the Snadd Formation. The V_p – Rho relationship is more unique (better end-member separation) than the V_p – V_s trend.

The stochastic forward modelling results for different fluid scenarios using the end-member depth trends as input are shown in Figure 6. The impact of compaction with increasing burial depth on fluid discrimination is illustrated using the Gaussian ellipses and 1D PDFs for AI and V_p/V_s ratio. Gaussian models are compared for brine, oil, and gas-filled sands with a 75% NTG. The centre of each Gaussian ellipse represents the mean for the class. The distance from the mean to the edge of the ellipse is equivalent to two standard deviations. At both modelled depths (1000 m and 2000 m TVD ML), there is a ~~general~~ significant overlap of the different fluid scenarios. The V_p/V_s ratio shows better discrimination compared to AI at both depth intervals. With increasing burial depth (i.e., at 2000 m TVD ML), we observe that the ellipses for the different fluid scenarios overlap much more. This is as expected because the rock framework becomes stiffer and it is more challenging to determine the pore fluid content. Such an analysis should be done for target reservoirs with contrasting burial depths such as the Snadd Formation, in order to determine the best set of elastic parameters to be used for interpretation at different depths of investigation. For very heterolithic formations with multimodal facies characteristics, the Gaussian assumption might be inadequate and non-parametric multivariate PDFs derived from point density contours in elastic space are more appropriate.

Figure 10 shows the RGB spectral blending flattened top Snadd Formation using iso-frequencies (11, 25, and 55 Hz for Red, Green, and Blue, respectively) decomposed from the full stack data through a Fourier transform operation. These frequencies ~~where~~ were selected based on the dominant frequency and slope changes in the amplitude spectrum. The dominant frequency from the spectral analysis is ~ 25 Hz. Some large – scale trends can be observed with the hot colours on the map. These bright yellow-red trends are interpreted to represent higher NTG intervals after comparing with the lateral NTG observed at the wells. A strong anomaly around Well-D corresponds with the anomalous sand proportion within the top of the Snadd Formation in the relay ramp area (Figure 3a). Most of the large – scale trends in the northern part of the study area have a NNE orientation (marked with dotted blue lines in Figure 11), except around Well-D with an almost E-W trend. Meanwhile in the southwestern part of the study area the dominant trend changes to ENE. The regional progradation of sediments from the Polar Urals was oriented SE-NW, but some local variations may have occurred around the study area in the Southern Hammerfest Basin (Glørstad-Clark et al., 2010; Klausen et al., 2014). Meanwhile, the E-W trends likely correspond with a locally sourced trend. The branching points along the TFFC (indicated with arrows in Figure 10) show some strong red anomalies with geometries consistent with point-sourced lobes where this major fault branches. The E-W trends and the anomalies tied to the TFFC might be indications of minor local Late Triassic tectonic activity along this master fault (Mulrooney et al., 2017). However, the fidelity of the flattening process is questionable in areas with dense faulting, which limits the resolution of the extracted anomalies, especially when dealing with very thin sands. A closer look into the details in a fault segment with less structuring reveals finer details of what we interpret to be a meandering channel, with a point bar complex. The width of these point bar complexes approximately range between 200 – 250 m. In a low NTG environment distal from the main source area, it is expected that the channels will develop mud-rich and stable levees, which help in confining the channel and therefore limiting the avulsion frequency. A schematic representation of the meander channel and point bar complex is also shown in Figure 11.

From a qualitative point of view, the seismic-to-well tie within the Snadd Formation is higher at the top and base of the formation. However, it is important to quantitatively assess the fit by examining the PEP and cross correlation over the interval of interest. In the example shown within Track 9 in Figure 12, the PEP is 78 % and the cross correlation is 88 % thus representing a good fit over the target zone.

Figure 11 also shows the comparison between the well logs and the results from both the facies – based Bayesian inversion and the neural network PHIE prediction at the reference well. The well log curves are shown in black, the predicted logs in red, and the blocky red logs within the same track represent the combined facies LFM output. There is a fairly good match between the inverted logs and the actual logs, especially for the thicker sand intervals. In contrast to a model-based deterministic inversion (with the LFM constructed from structurally guided well interpolation), the QC is not compromised because the LFM is not supplied but computed during the inversion. The difference (i.e., residuals) between the inverted traces and the actual seismic trace are also shown in Track 12 in Figure 11 for visual comparison.

The limitations in the seismic bandwidth and the effects of upscaling are more apparent when comparing the derived facies model (Track 7) to the unscaled (Track 5) and upscaled well log facies (Track 6) presented in Figure 11. In this example, there is a good match in the predicted sand units approximately ≥ 15 m. The prior probability for reservoir sand and non-reservoir (Track

8) within the upper part of the Snadd Formation was set as equal. Some smoothing was applied to the prior probabilities (seen as a step pattern on the prior probability curves) to account for gradational facies changes. In addition, the prior probability for reservoir sand is set to decrease towards the base of the Snadd Formation; this is consistent with geologic prior information about the vertical NTG distribution in the available wells. As expected, sand units smaller than 10 m are hardly present in the upscaled facies log and are equally not detected in the inverted facies model. The final facies result is the maximum a posteriori (MAP) facies or most likely facies. In this binary system (reservoir and non-reservoir), this implies a facies probability greater than 50%. However, if more than two facies are being inverted for, it is important to remember that the MAP facies in the Bayesian classification could have a probability as low as 34%.

Figure 12a shows the training (black curve) and validation error (red curve) profiles for a multi-attribute analysis performed to determine the optimum set of attributes to use further in the neural network. Table 2 contains the final list of 10 attribute transforms used. The combined shear Impedance (SI) LFM from the inversion showed the best individual correlation to PHIE. A ~~general~~ well-known problem for neural networks is the potential to over classify the training data set. One way to address this ~~challenge~~challenge is to start the analysis with a multi-attribute set that results in the smallest validation error (i.e., the lowest turn around point in the validation error profile). The average training error for all wells decreases with successive addition of attributes to the analysis. The lowest minima in the validation error profile occurs at the 10th attribute transform. Each data point on the validation error is obtained leaving out a target well in the analysis and using the other wells to predict the desired property. If more than 10 attributes are used, the prediction quality starts to decrease and we start over classifying the data, i.e., the point at which the average well training error keeps reducing while the validation error progressively increases.

Figure 12b shows a cross plot between the neural network predicted PHIE and actual PHIE log for five wells. The cross correlation between them is 0.67. This plot highlights the underlying challenge in predicting thin, below-resolution clean sand intervals. This challenge is common to the inversion and the neural network result. The prediction does not fully capture the upside in the PHIE estimates. No predicted PHIE data points are observed above 0.2. This is partly due to the sampling rate (4 ms) used in the training which is rather coarse (i.e., for thin high PHIE sand intervals within the Snadd Formation), but consistent to the seismic sampling rate. Track 4 in Figure 11 shows the comparison between the neural network predicted log (red) and the well log (black). The predicted log fully captures the PHIE trend in the log, and is consistent with the inverted facies (Track 7) at the well location.

An arbitrary line (Figure 13) through the reference well and a blind deviated well (i.e., well neither used in the depth trend for the inversion nor in the training for PHIE) validates the inversion and neural network results away from well control. In Figure 13a, the low AI layers ~~generally~~ correlate well to reservoir sand facies (Figure 13b) with relatively higher PHIE (Figure 13c) within the upper part of the Snadd Formation. The quality of the facies prediction can be quantified using a confusion matrix. The off-diagonal elements in the matrix indicate the degree of error. The confusion matrices for both wells are displayed in Figure 13b below the corresponding well. For the reference well, the facies aware inversion correctly classifies the reservoir facies of interest 87.5 % of the time and wrongly classifies it as non-reservoir 12.5 % of the time. The facies prediction for the deviated blind well, which was not included in defining the facies depth trends, is also shown. The reservoir sand prediction success is 65.38 %. This well has thinner sand units compared to the reference well, and this could be one reason for a lower classification success. In reservoirs where the facies do not show separate clusters in a rock physics space, the wavelet scaling becomes more crucial to the inversion result. However, the White (1980) method provided the appropriate wavelet scaling required in our case. Notice that the middle to lower section of the Snadd Formation (Figure 13c) is dominated by PHIEs < 0.1 and is correctly classified as non-reservoir (Figure 13b) in the facies-based inversion. Despite the upside limitation in the predicted PHIE result, it is still very useful in a qualitative sense when combined with the inverted facies, to highlight the cleanest intervals within the predicted reservoir sands in the upper parts of the Snadd Formation.

Figure 14 shows a horizon slice for PHIE and facies at the top of the Snadd Formation interval. The ovals and arrows from the RGB flattened slice in Figure 10 are shown for a visual qualitative comparison between the attributes. The extent of the anomalies indicating gross depositional trends (Figure 10) are much larger than observed in the PHIE (Figure 14a) and Facies (Figure 14b) horizon slices. In general, there is consistency between the PHIE and Facies horizon slices with a few exceptions. The large white ovals in Figure 14 show areas with predicted reservoir sand but with very low porosity predictions. This could be interpreted to represent more cemented sands, as this area structurally lower (easily seen in Figure 3b around the grey arrow) within a graben structure bounded by relay ramp faults. The combined map (Figure 14c) showing the clean sand geobodies represent predicted sand facies with PHIEs > 15 %. Artefacts are produced along the faults in both the facies and PHIE maps and reliability of the maps increase away from the faults.

CONCLUSION

Properly constrained facies-dependent rock physics depth trends are very important for successful quantitative seismic reservoir characterisation within the Snadd Formation in the Goliat field.

However, if these trends are to be used in other parts of the SW Barents Shelf, an appropriate reference depth needs to be thoroughly investigated before hanging the depth trends in areas with seismic data but no wells. Fluid sensitivity is shown to decrease with depth based on the PDFs obtained from the end member trends. Spectral decomposition and RGB blended results reveal two main depositional trends: i) a NNE trend compared to the SE – NW regional clinoform progradation of sediments from the Uralide orogeny, and ii) an E-W local trend which likely represents local sources tied to pulses of sediments at branching points of the TFFC. The Snadd Formation is strongly compartmentalised so the fidelity of the flattened slice is uncertain in intensively faulted areas.

Despite the considerable overlap of the binary facies in a rock physics elastic space, the facies-aware Bayesian inversion is still able to largely discriminate reservoir sands from non-reservoir at a blind well (i.e., not used in the depth trend analysis). When inverting for more than two facies, it is crucial to further investigate the probability of the most likely facies which can be as low as 26% (i.e., if four facies are inverted for).

The neural network porosity predictions capture the general vertical trends in the wells, but do not properly capture the very thin high PHIE sands. However, the PHIE results are consistent with the inverted facies and can be used in a qualitative manner to discriminate the best reservoir facies with high PHIE. Areas interpreted to represent point sources for sediment input along the TFFC from the RGB flattened slice are supported by both facies and PHIE predictions. Neural networks should be viewed as an additional tool to decode complex relationships in the data especially when available linear and non-linear rock physics models fail.

Acknowledgements

This work is partly funded by the project “Reconstructing the Triassic Northern Barents shelf; basin infill patterns controlled by gentle sags and faults” (Trias North) under grant 234152 from the Research Council of Norway and with financial support from Tullow Oil Norge, Lundin Norway, Statoil ASA, Edison Norge and Dea Norge. We thank Eni Norge and Statoil ASA of the PL229 license for permission to publish the data, and Filippos Tsikalas (Eni Norge) for valuable discussions. This work has been carried out using RokDoc, HampsonRussell, and DUG Insight commercial software packages at the University of Oslo (UiO).

REFERENCES

Aki, K., and P. G. Richards, 1980, Quantitative seismology: Theory and methods: Freeman and Co.

Baig, I., Faleide, J. I., Jahren, J., and Mondol N. H., 2016, Cenozoic exhumation on the southwestern Barents Shelf: Estimates and uncertainties constrained from compaction and thermal maturity analyses. Marine and Petroleum Geology. ISSN 0264-8172. 73, s 105-130. doi: 10.1016/j.marpetgeo.2016.02.024

Buia, M., C. Cirone, J. Leutscher, S. Tarran, and B. Webb, 2010, Multi-azimuth 3D survey in the Barents Sea: First Break, 28, 65–69.

Castagna, J. P., H. W. Swan, and D. J. Foster, 1998, Framework for AVO gradient and intercept interpretation: Geophysics, 63, no. 3, 948–956, http://dx.doi.org/10.1190/1.1444406.

Cooke, D. A., and W. A. Schneider, 1983, Generalized linear inversion of reflection seismic data: Geophysics, 48, 665–676, doi: 10.1190/1.1441497.

Dalland, A., Worsley, D., Ofstad, K., 1988. A Lithostratigraphic Scheme for the Mesozoic and Cenozoic Succession Offshore Mid- and Northern Norway. Direktoratet, Stavanger.

Faleide, J. I., S. T. Gudlaugsson, and G. Jacquart, 1984, Evolution of the western Barents Sea: Marine and Petroleum Geology, 1, 123–150, IN1–IN4, 129–136, IN5–IN8, 137–150, doi: 10.1016/0264-8172(84)90082-5.

Gabrielsen, R.H.,1984, Long-lived fault zones and their influence on the tectonic development of the southwestern Barents Sea. Journal of Geological Society of London, 141, 651-662.

Gabrielsen, R.H., Færseth, R.B., Jensen, L.N., Kalheim, J.E. & Riis, F., 1990, Structural elements of the Norwegian Continental Shelf. Part I: The Barents Sea Region. Norwegian Petroleum Directorate Bulletin, 6, 33.

Gardner, G. H. F., L. W. Gardner, and A. R. Gregory, 1974, Formation velocity and density — The diagnostic basics for stratigraphic traps: Geophysics, 39, no. 6, 770–780, http://dx.doi.org/10.1190/1.1440465.

Gassmann, F., 1951, Elastic waves through a packing of spheres: Geophysics, 16, 673–685, doi: 10.1190/1.1437718.

Glørstad-Clark, E., J. I. Faleide, B. A. Lundschien, and J. P. Nystuen, 2010, Triassic seismic sequence stratigraphy and paleogeography of the western Barents Sea area: Marine and Petroleum Geology, 27, 1448–1475, doi: 10.1016/j.marpetgeo.2010.02.008.

Hampson, D. P., J. S. Schuelke, and J. A. Quirein, 2001, Use of multiattribute transforms to predict log properties from seismic data: Geophysics, 66, 220–236, doi: 10.1190/1.1444899.

Henriksen, E., A. E. Ryseth, G. B. Larssen, T. Heide, K. Rønning, K. Sollid, and A. V. Stoupakova, 2011b, Tectonostratigraphy of the greater Barents Sea: Implications for petroleum systems: Geological Society, London, Memoirs 35, 163–195.

Johansen, T. A., E. H. Jensen, G. Mavko, and J. Dvorkin, 2013, Inverse rock physics modeling for reservoir quality prediction: Geophysics, 78, no. 2, M1–M18, doi: 10.1190/geo2012-0215.1

Mørk, M. B. E., 1999, Compositional variations and provenance of Triassic sandstones from the Barents Shelf: Journal of Sedimentary Research, 69, 690–710, doi:10.2110/jsr.69.690.

Mulrooney, M.J., Leutscher, J., and Braathen, A., 2017, A 3D structural analysis of the Goliat field, Barents Sea, Norway. Marine and Petroleum Geology, 86, 192-212.

Ohm, S. E., D. A Karlsen, and T. J. F. Austin, 2008, Geochemically driven exploration models in uplifted areas: Examples from the Norwegian Barents Sea: AAPG Bulletin, 92, 1191–1223, doi: 10.1306/06180808028.

Kemper, M., and J. Gunning, 2014, Joint impedance and facies inversion — Seismic inversion redefined: First Break, 32, 89–95.

Klausen, T.G., Ryseth, A.E., Helland-Hansen, W., Gawthorpe, R., Laursen, I., 2014, Spatial and temporal changes in geometries of fluvial channel bodies from the Triassic Snadd Formation of offshore Norway. J. Sediment. Res. 84, 567e585.

Klausen, T. G., Ryseth, A. E., Helland-Hansen, W., Gawthorpe, N., Laursen, I., 2015, Regional development and sequence stratigraphy of the Middle to Late Triassic Snadd Formation, Norwegian Barents Sea: Marine and Petroleum Geology, 62, 102-122, doi.org/10.1016/j.marpetgeo.2015.02.004.

Pramanik, A. G., V. Singh, R. Vig, A. K. Srivastava, and D. N.Tiwary, 2004, Estimation of effective porosity using geostatistics and multiattribute transforms: A case study: Geophysics, 69, 352–372, doi: 10.1190/1.1707054.

Riis, F., B. A. Lundschien, T. Hoy, A. Mork, and M. B. E. Mork, 2008, Evolution of the Triassic shelf in the northern Barents Sea region: Polar Research, 27, 318–338, doi: 10.1111/j.1751-8369.2008.00086.x.

Sams, M., and Carter, D., 2017, Stuck between a rock and a reflection: A tutorial on low-frequency models for seismic inversion, Interpretation, 5(2), B17-B27.https://doi.org/10.1190/INT-2016-0150.1

Whitcombe, D. N., P. A. Connolly, R. L. Reagan, and T. C. Redshaw, 2002, Extended elastic impedance for fluid and lithology prediction: Geophysics, 67, 63–67, doi:10.1190/1.1451337.

White, R.E. [1980] Partial coherence matching of synthetic seismograms with seismic traces. Geophysical Prospecting, 28(3), 333-358.

Yenwongfai, H. D., N. H. Mondol, J. I. Faleide, and I. Lecomte, 2017a, Prestack simultaneous inversion to predict lithology and pore fluid in the Realgrunnen Subgroup of the Goliat

Field, southwestern Barents Sea: Interpretation, 5, no. 2, SE75–SE96, http://dx.doi.org/10.1190/INT-2016-0109.1.

~~Zoeppritz, K., 1919, On the reflection and penetration of seismic waves through unstable layers: Erdbebenwellen VIIIB, Goettinger Nachrichten 1, 66–84.~~

LIST OF FIGURES

Figure 1 Location map for the Goliat Field (adapted from NPD factmaps) in the Norwegian sector of the Barents Sea. The field is cut by the Troms-Finnmark Fault Complex within blocks 7122/7 and 7122/8 (Yenwongfai et al.,2017a)

Figure 2 Triassic chronostratigraphic framework comparison (a) for different authors. The subdivisions are based on 2nd and 3rd order sequences (Klausen et al., 2015). The Snadd Formation (target in this study) is also starred. The vertical change in the net-to-gross (as seen from the Sand Flag log track) effectively divides the interval into three main lithological zones (b).~~Notice the vertical change in the net-to-gross effectively dividing the interval into three main lithological zones (b).~~ Zone 1 has thicker more consistent sand units. Meanwhile zone 2 and 3 have heterolithic sands and shales respectively. ~~-~~Maximum flooding surfaces (MFSs) bounding the top and base of the Snadd Formation are also indicated. The P-impedance log is superimposed on the full stack seismic section. Note that positive amplitudes on the seismic represent soft events.

Figure 3 Well correlation profile from north to south. Well-D has an anomalous high sand proportion within the Snadd Formation and is located within a relay ramp structure (black arrow). Well-D is a side track from Well-G (not visible in Figure 3b) and deviates further away from Well-G below the top Snadd Formation horizon. Minor faults around both wells might explain differences in the observed NTG. Gamma log motifs from Well-B show good examples of stacked fining upward channels bounded by flooding surfaces.

Figure 4 ~~Summary w~~Workflow implemented for petrofacies and PHIE characterisation within the Snadd Formation. Depth trends play a central role in the feasibility study and during the inversion. The flow diagram shows the routes to ~~seismic facies characterisation.~~clean sand delineation. The five main steps in the seismic reservoir characterisation workflow are highlighted in green.

Figure 5: End-member depth trends for sand and shale through the whole well interval. The Vp, Vs, Rho, and PHIE trends are the primary trends (a) while the other trends (b) are derived from the primary trends. The sand-end member trends have been Gassmann fluid substituted to brine. The black circle shows the approximate depth location of the top Snadd Formation.

Figure 6: Depth varying PDFs (a) based on stochastic forward modelling of the end-member trends (shown in Figure 5). The plots show the fluid discrimination of AI and Vp/Vs attributes as a function of depth. Sensitivity decreases with depth as shown by increasing overlap of each ellipse and PDFs. Also the effective extended elastic impedance (EEI) chi angle (c) using the depth trends are also shown. The black and red arrows indicate the effective lithology and fluid angles.

Figure 7 AI versus Vp/Vs cross plots colour coded with Vsh (a) and PHIE (b). The contour density for sand and shale are based on a PHIE cut-off using 12% as the threshold. Sands dominate at low AI and Vp/Vs ratios. However, the histograms still show a significant overlap of both facies.

Figure 8 Reservoir and non-reservoir depth trends within the Snadd and kobbe Formation time interval. These depth trends (a) provide the uncertainty distribution (standard deviation of the derived trend curve) of the elastic properties as a function of depth as well as the cross correlation and constraints between the elastic parameters per facies. A cross plot comparison (b) between the prior model derived from the depth trends and the corresponding well data are also shown.

Figure 9 Wavelet processing and spectral analysis. The near, mid, and far angle stack wavelets (a) have all been extracted using the White (1980) method. The wavelets have been extracted based on the offset location with the highest PEP close to the well bore. The signal and noise spectra (b) at the top of the Snadd Formation interval are also shown with the selected frequencies used in the RGB blend.

Figure 10: Spectral decomposition and RGB blending of selected frequencies displayed at the top Snadd Formation flattened horizon slice. The corresponding frequency spectra (Figure 9b) is also inserted for reference to the frequencies. The bright red arrows show a dominant NNE trend. Meanwhile close to the branching points along the Troms-Finnmark Fault Complex (TFFC), observed anomalies are oriented E – W (black dotted lines). The white dotted lines, show the anomaly around Well-D (anomalous sand proportion in Figure 3) indicated with a blue arrow. A detailed view around Well-E shows a schematic representation of a channel and point bar complex. Note that Well-E just sits at the edge of this anomaly.

Figure 11: Facies-aware inversion and neural network results at the reference well. The inverted elastic logs (blue logs in Track 2 and 3) are plotted alongside the LFM (low frequency model) output logs (red logs) in the same tracks. There is a good match between the inverted facies log (Track 7) compared to the upscaled (Track 6). The inversion synthetic logs and the residuals are

also shown in Track 11 and Track 12. The predicted PHIE log (red) from the neural network shows a match to the thicker and better developed reservoir sands (above 1240 ms TWT).

Figure 12 Multi-attribute neural network training (a) and prediction correlation (b). The validation error is shown to increase after the 10th attribute transform in the multi-attribute analysis. Attribute number 1 – 10 are used in the neural network prediction. We refer the reader to Table 2 for more details in Figure 12a.

Figure 13 Arbitrary line section through the reference well (Well-A) and the blind well (Well-C). The simultaneous Bayesian Joint Impedance (a) and Facies (b) inversion results are compared with the neural network PHIE predictions (c). Good PHIEs observed at the upper part of the Snadd Formation (results from the neural network) are consistent with the predicted reservoir sands from the inversion. The quality of the facies predictions are illustrated in a confusions matrix below the respective wells. Diagonal elements in the matrix indicate the degree of success of the classification.

Figure 14 Horizon slices at the top of the Snadd Formation for effective porosity (a) and binary facies (b) over a 30ms window. The binary facies map is the result from the facies-based inversion, while the the porosity map is the output from the multi-layer feedforward neural network. The clean sand geobodies (c) represent predicted reservoir sand facies with PHIE greater than 15 %. Reservoir delineation is improved by qualitatively combining areas with good effective porosity in regions where reservoir sand is predicted by the inversion. The arrows and ovals from the flattened RGB slice in Figure 10, are inserted for visual comparison.

Formatted: Justified

LIST OF TABLES

Table 1: Grain and fluid properties used as input for brine substitution of the sand end-member trend through Gassmann's equation. Quartz properties have been used for sand end-member grain properties.

Table 2: Multi-attribute transform list used as input to the neural network. Attribute numbers correspond to numbers used in Figure 13a. The attribute transform with the highest individual correlation to PHIE, is the Shear Impedance (SI) LFM output constructed during the inversion. Note that the errors associated with each successive is attribute is cumulative by applying all preceding attributes.

EAGE Publications
Journal Submission Form

By signing this form the undersigned (hereinafter: **Author**) grants EAGE Publications B.V. (hereinafter: **Publisher**) the exclusive publication rights regarding author's publication specified below (hereinafter: the **Work**).

Note: this concerns Publisher's standard journal submission form. Other forms are available for (green and golden) Open Access licenses. In case the Author's Work results from research funded (wholly or in part) with public funds, or if the Author made the Work as an employee of a university or a publicly funded research institute, please inform the Publisher accordingly.

The Author

Name:
Address:
E-mail:
Names of co-authors (if applicable):
Name and address of the owner of the Intellectual Property Rights (if applicable):

The Work

Title:

The Journal:

Name of the Journal: [to be filled in by EAGE]

Author declares the following

1. Publishing rights

1.1. Author hereby grants to Publisher the exclusive (also to the exclusion of Author) publishing rights in relation to the Work. To this effect, Author grants Publisher a worldwide exclusive perpetual and non-cancellable license to all Intellectual Property Rights regarding the Work.

1.2. The publishing rights as defined in clause 1.1. include – but are not limited to – the following:

(i) the right to make the Work available to the public in print or in digital format, including – but not limited to – the right to publish the Work in the Journal mentioned above and other journals of Publisher, and through any of its digital platforms including EarthDoc;

(ii) the right to promote, sell, distribute or otherwise (commercially) exploit the Work;

(iii) the right to make the Work fit for publication, including the right to amend the layout and title and to translate the Work in any language;

Initial Author: HDY

(iv) the right to duplicate the Work;

(v) the right to grant (sub)licenses to third parties and to engage the services of third parties, explicitly including the companies within the group structure of Publisher;

(vi) the right to register the Work with collective rights organizations (such as the Copyright License Agency (UK), the Copyright Clearance Center (USA) and Stichting Pro/Stichting Reprorecht (the Netherlands);

(vii) any future and/or currently unknown means of exploitation of the Work by Publisher.

1.3. The term **Intellectual Property Rights** has the following meaning: all worldwide intellectual property and similar or related rights in the broadest sense of the term, or any entitlement thereto, especially those including – but not confined to – (1) copyrights, (2) portrait/image rights, (3) database rights, (4) design rights, (5) trademark rights, and (6) knowhow – including all powers related to these intellectual property rights, such as the exclusive rights to reproduce and make available to the public – and including any future Intellectual Property Rights, which is also deemed to refer to all entitlements which relevant national and international legislation accords or may accord to them.

1.4. The name of the Author and (if applicable) the name of the co-authors and/or owner of the Intellectual Property Rights as filled in above will be mentioned in the published Work, unless this cannot be reasonably be required.

1.5. This form constitutes a documented license [akte] as referred to in clause 2 under 3 of the Dutch copyright act [Auteurswet]. The Author shall cooperate at first request of EAGE and free of charge with the fulfilment of any legal formalities required for the grant of license.

2. Delivery and acceptance

2.1. Author agrees to deliver to Publisher a complete draft of the Work. This includes the text of the Work in Word format and all other materials (such as images, data, tables, diagrams, graphics, maps or any other illustrative material) in electronic form. Any delivered materials should be in publishable (high resolution) format and comply with Publisher's guidelines as published on Publisher's website.

2.2. If the Work contains any materials (see examples in the previous clause) that are not created by Author or to which any third party can claim any Intellectual Property Rights or other rights, Author will provide Publisher with a written confirmation from such party that these materials may be used by Publisher and a royalty-free license is provided therefore.

2.3. If the Work contains quoted texts from other works these quotes need to comply with the copyright legislation applicable to quotes. At least the following conditions apply: the quoted work has already been lawfully published, only a reasonable portion of the original work is quoted, the persona rights of the original authors are respected, a proper reference to the original work is made in the foot notes, and the quote is used with a legitimate interest – for instance to discuss the quoted material or support the statements of the Author.

Initial Author: HDY

2.4. Publisher has the right to decide at its sole discretion not to publish the Work or to cease/withdraw the publication of the Work, in which case Publisher is not liable for any costs and/or damages resulting from this decision.

2.5. In case Publisher confirms that the Work will not be published in the Journal mentioned above, the license pursuant to article 1 will become non-exclusive. This means that the Author is allowed to publish the Work elsewhere.

3. Royalty-free license

The publication rights and license as defined in article 1 of this form concerns a royalty-free license, which means that Author is not entitled to any compensation. Author agrees with a royalty-free license because the Publisher gives the Author the opportunity to publish his Work in a renowned journal and the Publisher does not charge any costs for this publication, for instance for editing or adding (colour) pictures to the Work.

4. Warranties and indemnities

4.1. Author undertakes and warrants that nothing prohibits the publication and exploitation of the Work pursuant to the license granted under article 1 of this form. More specifically, Author undertakes and warrants that:

(i) Author either owns, or is entitled to the use on the basis of a documented license, all Intellectual Property Rights or other rights pertaining to the Work and all materials included in the Work. In case the Author is entitled to use the Intellectual Property Rights on the basis of a license (for instance in case the employer is the owner), the Author will prove this (for instance by providing a copy of a written agreement, a written confirmation or a signature of approval under this form). In case of co-authors, article 7 of this form applies;

(ii) no regulations regarding Open Access apply to the Work, for instance because the Author's Work results from research funded (wholly or in part) with public funds, or the Author made the Work as an employee of a university or a publicly funded research institute;

(iii) the Work has not been published before, nor that any license to publish the Work has been granted to any other party;

(iv) no rights of third parties, including but not limited to Intellectual Property Rights or any civil rights, will be infringed by the publication or exploitation of the Work;

(v) the Work does not contain any libelous matter and the Work is not defamatory or obscene;

(vi) the Work does not contain any faulty or illegal information or information that brings Publisher or other third party into disrepute.

Initial Author: HDY

4.2. Author shall fully indemnify Publisher and hold Publisher harmless for any costs and damages (direct or indirect) of Publisher in case of any non-compliance with the warranties mentioned in this article.

4.3. Author is fully responsible and liable for the contents of the Work. Publisher shall have no obligation to verify the contents of the Work or any other materials supplied by Author or to verify if publication thereof may cause any damages to (third) parties. The decision of Publisher to publish the Work or any other approval of the Work shall not be construed as an approval of the contents or confirmation of its legality.

5. <u>Liability</u>

5.1. To the fullest extent permitted by law, Publisher shall under no circumstances be liable for any indirect, consequential, special, exemplary, incidental or punitive damages, such as loss of (future) profits or other economic loss, damages for delay, third party claims and suchlike.

5.2. Publisher's total liability – including liability arising out of the publication of the Work, negligence, tort or warranty – shall be confined to the amount as paid out by the liability insurance of Publisher in the case concerned, and in case such damages are not insured or paid by the insurance company the total liability from Publisher towards Author shall be confined to an amount of € 50,000.00 (fifty thousand euros).

6. <u>Infringement of Intellectual Property Rights</u>

If the Intellectual Property Rights pertaining the Work are infringed, Publisher is granted the right to take such legal action as may be required to restrain such infringement or to seek damages and claim the profits made by the infringing party therefore. Such actions shall be taken at the sole discretion of Publisher and at its own cost and expense. Publisher is not obliged to take any legal action. Author herewith grants Publisher a power of attorney to take such legal measures. If Author wants to take legal actions on Author's own account, parties will discuss the approach of such matter.

7. <u>Multiple authors</u>

In case the Work is written by multiple authors as indicated by the Author of page 1 of this form, Author warrants that its co-authors agree with the publication and exploitation of the Work pursuant to article 1 of this form. Notwithstanding this warranty, Author will ensure that its co-authors will also sign this form.

8. <u>Miscellaneous</u>

8.1. Publisher is allowed to assign its rights and obligations granted in this form to a third party, including a company within its group structure (for instance a mother, daughter or sister company). Author will – for as far as necessary – cooperate with such assignment.

8.2. This form shall be binding upon and inure to the benefit of the heirs, executors, administrators and assigns of Author, and upon and to the successors and assigns of Publisher.

8.3. This form is solely governed by and construed in accordance with the laws of the Netherlands. The application of the United Nations Convention on Contracts for the International Sales of Goods is precluded.

8.4. Any dispute arising between Author and Publisher pursuant or otherwise in relation to this form, which is deemed to include any that is regarded as such by either party, shall be resolved as much as possible through close consultation. In the event that parties are unable to resolve the dispute, it shall be adjudicated by a competent court of law in the city of Utrecht, the Netherlands, unless Publisher chooses to institute proceedings against Author before a competent court of law in Author's country of residence.

Thus agreed and signed by Author,

____
Date: 18/10/2017
Place: OSLO, Norway

Initial Author: HDY